

Algorithm and Realization of Robotic end Orientation Equivalent Similarity Transformation Based on Rodrigues

Juqing Yang

Key Laboratory of Photoelectric Imaging Technology and System, Ministry of Education of China, Beijing Institute of Technology, Zhuhai
Zhuhai, China
e-mail: yangjuqing@aoe.ac.cn

Wei Cao

Key Laboratory of Photoelectric Imaging Technology and System, Ministry of Education of China, Beijing Institute of Technology, Zhuhai
Zhuhai, China
e-mail: 17303@bitzh.edu.cn

Qiuji Zhou

Key Laboratory of Photoelectric Imaging Technology and System, Ministry of Education of China, Beijing Institute of Technology, Zhuhai
Zhuhai, China

Zhanhao Yi

Key Laboratory of Photoelectric Imaging Technology and System, Ministry of Education of China, Beijing Institute of Technology, Zhuhai
Zhuhai, China

Abstract—In the process of robotic pose measurement, error estimation and online correction, the relative pose transformation and calibration between coordinate frames are required. This paper presented a solution algorithm for measuring and precision evaluating the robot end orientation. Robotic frames transformation relationship was investigated. In view of the measuring space restricted problems of a robot end orientation, the unified description model of the robot end tool orientation transformation and the 3D coordinate measurement parameters of the space target are established. The algorithm of the robot end orientation using multi-point measurement is given with the coordinate frame equivalent similarity transformation. This algorithm utilizes the multi-point laser measurement values of the space rigid body to implement the spatial point coordinate center registration. By the least square optimization algorithm based on Rodrigues matrix transformation, the orthogonal rotation matrix of the orientation relative transformation can be obtained. At last the exact estimation of the robot end orientation z-y-x Euler angle and the orientation error are realized.

Keywords—orientation solution algorithm; equivalent similarity transformation; spatial coordinate center registration; Rodrigues matrix transformation

I. INTRODUCTION

In modern advanced manufacturing industry, industrial robots are widely used as the automatic intelligent manufacturing equipment. Due to its poorer space absolute positioning accuracy, the robot kinematics calibration needs to be implemented using precision device for measuring and obtaining the end tool sampling point space coordinates and the end tool pose relative to the robot base frame. After comparing them with the end orientation nominal values of the robot controller, the best fitting values of the kinematic parameters can be evaluated [1, 2].

There are many ways to describe the frame orientation, the most common methods are Euler angle, orthogonal rotation matrix and Hamilton quaternion [3, 4]. High-precision orientation measurement methods, which are commonly used, include laser tracking measurement or visual image measurement. The visual system measures the target mark by adopting monocular or binocular image-forming principle, which has the characteristics of fast measuring speed and suitable for non-contact dynamic measurement environment [5, 6].

However, the initial calibration and estimation algorithm of visual system are more complex, and the identification and coding process of the imaging points are generally needed to solve the target orientation parameters [7]. The laser tracking measurement system has the advantages of large measuring space, high measuring accuracy, fast measuring speed, multi functions, strong universality and real-time characteristic, which is suitable for industrial measurement environment [8].

Above orientation evaluating methods have great limitations in the robot end motion space, which cannot obtain the orientation transformation result and error of the robot in extended workspace domain [9]. During the existing calibration process, the measurement range of a robot end orientation is generally allowed within the range of ± 30 degree of the laser incidence angle. Therefore, the global error parameter can only be measured and calibrated by the position coordinate error or distance precision.

Aiming at the shortcomings of above orientation algorithm methods, this paper presented a robot coordinate frame equivalent similarity transformation algorithm based on Rodrigues. Then, the end position and orientation error of the robot are obtained by using the laser measurement value of the space rigid multi-point positions, and the accurate evaluation of the rotation matrix and errors of the robot end tool are performed.

II. MEASUREMENT MODEL

The relative orientation transformation of the robot end tool can be attributed to the spiral transformation between two concurrent coordinate frames. The robot end orientation can be obtained by the rotation transformation of two rigid body coordinate systems.

Three measuring points P_1, P_2 and P_3 are marked on the end tool coordinate frame, and the three points are required to be non-collinear which is considered as an equivalent rigid body. The orientation transformation measuring coordinate system is established. The laser tracking measurement coordinate frame is the reference frame $\{L\}$, the orientation azimuth of the end tool frame $\{E\}$ is consistent with the end-flange coordinate frame $\{6\}$, and the target point P_1 is the origin of the end tool coordinate frame. The coordinates of the target points are P_{10}, P_{20} and P_{30} at the robot's initial joint configuration. The homogeneous transformation matrix of the end tool coordinate frame relative to the base coordinate frame is T_{E0}^B . After controlling the robot to a new position, the coordinates of the target point change to be P_{11}, P_{21} and P_{31} . The corresponding homogeneous transformation matrix of the end tool coordinate frame relative to the base coordinate frame changes to be T_{E1}^B .

A coordinate frame equivalent transformation model is set up. When the end tool coordinate frame changes to $\{E1\}$ from $\{E0\}$, it can be equivalent to remain the same, transform the robot base frame $\{B\}$ and the measuring coordinate system $\{L\}$ respectively, build a new equivalent robot base frame $\{B1\}$ and an equivalent measurement coordinate frame $\{L1\}$. The equivalent transformation model of the coordinate frame is shown in Figure 1.

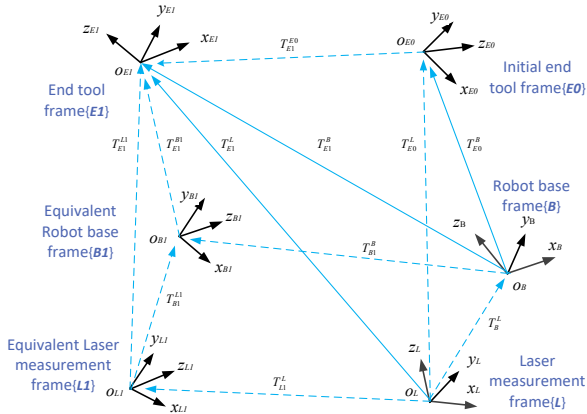


Figure 1. Equivalent transformation model of robot frame.

At this point, the orientation matrix relationship between the end tool coordinate frame $\{E1\}$ relative to the robot equivalent base coordinate frame $\{B1\}$ and the equivalent measurement coordinate frame $\{L1\}$ is the same with that $\{E0\}$ relative to the robot coordinate frame $\{B\}$ and the measuring coordinate frame $\{L\}$.

That is:

$$T_{E0}^B = T_{E1}^{B1}; T_{E0}^L = T_{E1}^{L1} \quad (1)$$

At the same time, we can say that the orientation rotation transformations between the end tool frame and the base frame as well as the measurement frames are similarity transformation, whose rotation transformation matrixes are of the similarity. That is:

$$R_{E0}^B = R_{E1}^{B1} \quad (2)$$

According to the above equivalent principle of similarity transformation frame, the end tool point coordinates P_{10}, P_{20}, P_{30} and P_{11}, P_{21}, P_{31} can be respectively regarded as the composed rigid body measurement coordinate of the points P_1, P_2, P_3 in the laser coordinate frame and the equivalent laser measurement frame. Therefrom, this can be used to correlate the end tool orientation of the robot different joint configuration by above fixed point coordinates. Then, the corresponding coordinate transformation relation can be transformed into the transformation solution of the concurrent rigid body coordinate frame.

III. ESTIMATION ALGORITHM OF ORIENTATION RELATIVE TRANSFORMATION

Measure the coordinates of the same set of sampling points in two coordinate systems respectively, and match the two coordinate systems' orientation relevance by sampling points. Because the sampling points are the same in different coordinate frames, the combination of these sampling points can be used as the equivalent rigid body. According to the invariant theory of the rigid body barycentric coordinates, using the gravity centroid criterion method to configure the center of gravity space for each sample point coordinates, the distance to the center of gravity is constant at various points on the equivalent rigid body, and each point's corresponding distance is equal. That is shown as Figure 2.

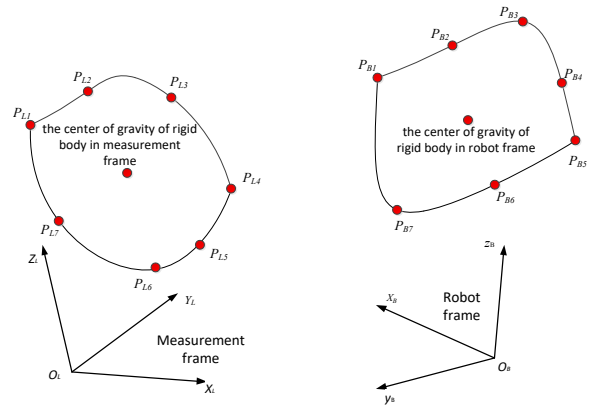


Figure 2. Equivalent rigid body in different coordinate frames.

Using the invariant of the rigid body barycentric coordinates, configure the fixed point coordinate's centralized barycenter space adopting the gravity criterion method, remove the coordinate offsets of homogeneous transformation relations, reduce the robot localization error and measurement error, directly get the rotation transformation description. The spatial registration center of

gravity coordinates of the end tool target point P_1, P_2 and P_3 in two coordinate systems can be expressed respectively:

$${}^L P_g = \begin{bmatrix} x_{Lg} = \frac{\sum_{i=1}^3 x_{i0}}{3} \\ y_{Lg} = \frac{\sum_{i=1}^3 y_{i0}}{3} \\ z_{Lg} = \frac{\sum_{i=1}^3 z_{i0}}{3} \end{bmatrix}; {}^{L1} P_g = \begin{bmatrix} x_{L1g} = \frac{\sum_{i=1}^3 x_{i1}}{3} \\ y_{L1g} = \frac{\sum_{i=1}^3 y_{i1}}{3} \\ z_{L1g} = \frac{\sum_{i=1}^3 z_{i1}}{3} \end{bmatrix} \quad (3)$$

In the upper left of the variable, L and $L1$ represent the center of gravity in the laser measurement coordinate frame and the equivalent laser measurement coordinate frame respectively. The barycentric coordinate conversions of the fixed points are carried out as

$$P_{gi0} = P_{i0} - {}^L P_g = \begin{bmatrix} x_{i0} - x_{Lg} \\ y_{i0} - y_{Lg} \\ z_{i0} - z_{Lg} \end{bmatrix} = \begin{bmatrix} x_{gi0} \\ y_{gi0} \\ z_{gi0} \end{bmatrix} \quad (4)$$

$$P_{gi1} = P_{i1} - {}^{L1} P_g = \begin{bmatrix} x_{i1} - x_{L1g} \\ y_{i1} - y_{L1g} \\ z_{i1} - z_{L1g} \end{bmatrix} = \begin{bmatrix} x_{gi1} \\ y_{gi1} \\ z_{gi1} \end{bmatrix} \quad (5)$$

P_{gi0}, P_{gi1} are the equivalent centroid coordinate points of the fixed point P_i in the laser measurement frame and the equivalent laser measurement frame respectively.

After the gravity spatial registration, the orientation transformation matrix can be solved according to the fixed point relationship, R_{L1}^L is the orientation rotation matrix between the laser measurement coordinate system $\{L\}$ and the equivalent laser measurement coordinate system $\{L1\}$.

The corresponding rotation transformation relation of the coordinate system after the center of gravity registration is shown as follows:

$$P_{gi0} = \begin{bmatrix} x_{gi0} \\ y_{gi0} \\ z_{gi0} \end{bmatrix} = R_{L1}^{L0} \cdot \begin{bmatrix} x_{gi1} \\ y_{gi1} \\ z_{gi1} \end{bmatrix} = R_{L1}^{L0} \cdot P_{gi1} \quad (6)$$

Establish Rodrigues matrix equation to transform and solve the parameters of rotation matrix of the robot end frame. Set up the anti-symmetric matrix S , R_L^B can be expressed as the Rodrigues matrix equation form:

$$R_L^B = (E - S)^{-1} \cdot (E + S) \quad (7)$$

where,

$$S = \begin{bmatrix} 0 & -c & -b \\ c & 0 & -a \\ b & a & 0 \end{bmatrix}$$

a, b and c are the Rodrigues parameters, and E is the third-order unit matrix. There is,

$$(E - S) \cdot \begin{bmatrix} x_{Bgti} \\ y_{Bgti} \\ z_{Bgti} \end{bmatrix} = (E + S) \cdot \begin{bmatrix} x_{Lgti} \\ y_{Lgti} \\ z_{Lgti} \end{bmatrix} \quad (8)$$

Expand the equation set, extract a, b , and c , write them as vectors. By applying the Rodrigues matrix transformation, the solving equations can be set up:

$$\begin{bmatrix} 0 & z_{gi0} + z_{gi1} & y_{gi0} + y_{gi1} \\ z_{gi0} + z_{gi1} & 0 & -x_{gi0} - x_{gi1} \\ -y_{gi0} - y_{gi1} & -x_{gi0} - x_{gi1} & 0 \end{bmatrix} \cdot \begin{bmatrix} a \\ b \\ c \end{bmatrix} = \begin{bmatrix} -x_{gi0} + x_{gi1} \\ -y_{gi0} + y_{gi1} \\ -z_{gi0} + z_{gi1} \end{bmatrix} \quad (9)$$

Substitute three groups of target points coordinates into (9) to form overdetermined system of equations, apply least squares method to solve the generalized inverse, calculate the values of a, b, c . After substituting the solution results into Rodrigues matrix and (7), R_{L1}^L , the equivalent conversion rotation matrix of the laser measuring frame can be calculated out when the robot joint configuration is changed to arbitrarily configuration m1. The rotation matrix has the orthogonality at the same time.

According to the similarity transformation method, the equivalent conversion process of the laser measurement frame and the robot base frame are similar, the rotation matrix R_{L1}^L and R_{B1}^B are similar too, thus we can obtain:

$$R_{B1}^B = (R_B^L)^{-1} \cdot R_{L1}^L \cdot R_B^L \quad (10)$$

The similarity transformation matrix R_B^L is the rotation matrix of the robot base frame relative to the laser measuring frame, which needs to work out in advance, and its calibration and calculation process is no longer detailed in this paper.

For relative orientation transformation matrix of a robot end tool frame R_{T1}^{T0} , it is the similarity transformation, namely

$$R_{E1}^{E0} \cong R_{B1}^B \quad (11)$$

Substitute formula (10) into (11), we can obtain the following formula:

$$R_{E1}^{E0} = (R_{E0}^B)^{-1} \cdot R_{B1}^B \cdot R_{E0}^B = (R_{E0}^B)^{-1} \cdot (R_B^L)^{-1} \cdot R_{L1}^L \cdot R_B^L \cdot R_{E0}^B \quad (12)$$

It can be found that when the robot is in the joint configuration of m1, the actual orientation rotation matrix of the end tool is shown:

$$R_{E1}^B = R_{E0}^B \cdot R_{E1}^{E0} = (R_B^L)^{-1} \cdot R_{L1}^L \cdot R_B^L \cdot R_{E0}^B \quad (13)$$

Finally, the orientation matrix error is obtained by comparison with the nominal orientation rotation matrix calculated by kinematics. According to the above calculation process, we can theoretically evaluate the orientation error of the end tool at any position.

IV. ALGORITHM IMPLEMENTATION AND RESULTS

According to the relative transformation resolving method of robot end orientation, the orientation rotation matrix measurement and comparison experiment were carried out. The laser tracking equipment, 6-DoF laser target, laser reflection ball target and KUKA KR16-2 robot are used as experimental devices, as shown in Figure 3.

Run the robot back to the Home location as the initial joint configuration, the six-degree freedom laser target is fixed to the robot end-flange. The transformation matrix T_B^L can be solved according to the robot base frame conversion optimization evaluation method.

$$T_B^L = \begin{bmatrix} -0.917568 & 0.397561 & -0.003676 & 5120.6247 \\ -0.397573 & -0.917566 & -0.002706 & -1113.084 \\ -0.002297 & 0.004299 & 0.99999 & -706.9113 \\ 0 & 0 & 0 & 1 \end{bmatrix}$$

TABLE I. TESTING CONTRAST OF RELATIVE TRANSFORMATION OF END ORIENTATION

	multi-point solution value of orientation relative transformation (z-y-x)			six degrees of freedom target measurement orientation (z-y-x)		
	φ_z (deg)	φ_y (deg)	φ_x (deg)	φ_z (deg)	φ_y (deg)	φ_x (deg)
1	19.9682	0.0878	0.0579	19.7963	0.0825	0.0895
2	-179.8601	50.0214	-179.7059	-179.9408	50.0614	-179.9182
3	121.7833	89.9541	111.7991	121.5725	89.7523	112.1203
4	0.2679	79.9296	0.2238	0.2934	80.1231	0.2325
5	-89.8045	80.0294	-89.8064	-89.8541	80.0388	-89.5604
6	3.5778	70.5174	3.3225	3.5456	70.2541	3.5412
7	-89.8326	70.0314	-89.8417	-89.8251	70.2104	-89.8021
8	-96.6587	60.3983	-112.3941	-96.8745	60.5874	-112.5469
9	176.4027	69.6829	176.5646	176.4254	69.5428	176.2459
10	12.2882	89.9589	2.2054	12.2865	89.9589	2.2037



Figure 3. Testing relative transformation of end orientation.

It can be seen from the comparative test in the table that the estimated results by the robot end orientation relative transformation are very close to the measurement orientation angle with the 6-DoF laser target. It is shown that the equivalent similarity transformation method of the multipoint laser measurement can be used to reliably evaluate the orientation of the robot end tool frame.

V. CONCLUSION

In view of the constraint problems of target space position limited by laser tracking system for measuring robot end orientation, this paper presented an orientation transformation estimation algorithm. Using the equivalent similarity transformation method of coordinate system, the

Select 10 sets of the robot measurement positions and the corresponding joint configuration, control the robot to run to each orientation respectively, measure and record each group under the position of three ball target coordinates in turn, calculate the end tool orientation matrix using formula (6). The actual value of the rotation matrix of the end tool frame at the initial joint configuration is calculated by using the rotation component R_B^L in the above calculation results. The six degrees freedom target orientation were measured and recorded at 10 groups of robot joint configuration. Then the measurement results and above estimation results are converted into z-y-x Euler angles, the comparisons of orientation angle are shown in the following table 1.

unified description model between a robot end tool orientation transformation and the space target 3D coordinate measurement parameters is established. As a kind of compensating computation method, the coordinate frame orientation conversion algorithm achieved fast accurate solution of the rigid body coordinate transformation equation based on Rodrigues transformation matrix. The algorithm avoided the linearization of the rotation parameters, and the whole calculating process was simple and quick.

Through the barycentric registration of the space point coordinates and resolving of the least squares optimization algorithm based on Rodrigues matrix transformation, the orthogonal rotation matrix of the relative transformation orientation can be obtained, the experimental results verify the validity of the orientation algorithm. The coordinate system equivalent similarity transformation method based on multi-point laser measurement is adopted, which needs manually auxiliary measurement, but the relative transformation of the robot end orientation can be estimated and calibrated in much greater range.

ACKNOWLEDGMENT

This work is supported by the Science and Technology Service Network Initiative of the Chinese Academy of Sciences (Grant: KFJ-SW-STS-154), in part by the Research and Development Fund of Beijing Institute of Technology, Zhuhai (No. XK-2018-04, XK-2018-07 and XK-2019-01).

REFERENCES

- [1]" Y. Guo, S.B. Yin, Y.J. Ren, J.G. Zhu, S.R. Yang, S.H. Ye, A multilevel calibration technique for an industrial robot with parallelogram mechanism, *Precision Engineering-Journal of the International Societies for Precision Engineering And Nanotechnology*, 40 (2015) 261-272.
- [2]" J.D. Barnfather, M.J. Goodfellow, T. Abram, A performance evaluation methodology for robotic machine tools used in large volume manufacturing, *Robotics And Computer-Integrated Manufacturing*, 37 (2016) 49-56.
- [3]" W. Wang, F. Liu, C. Yun, Calibration method of robot base frame using unit quaternion form, *Precision Engineering-Journal Of the International Societies for Precision Engineering and Nanotechnology*, 41 (2015) 47-54.
- [4]" M. Fan, X. Han, Precision improvement method for serial robot localization based on a new calibration and compensation strategy, *Journal of Beijing University of Aeronautics and Astronautics*, 43 (2017) 176-183.
- [5]" L. Wu, H. Ren, Finding the Kinematic Base Frame of a Robot by Hand-Eye Calibration Using 3D Position Data, *Ieee Transactions on Automation Science And Engineering*, 14 (2017) 314-324.
- [6]" Y. Wu, A. Klimchik, S. Caro, B. Furet, A. Pashkevich, Geometric calibration of industrial robots using enhanced partial pose measurements and design of experiments, *Robotics And Computer-Integrated Manufacturing*, 35 (2015) 151-168.
- [7]" J.C. Bazin, C. Démonceaux, P. Vasseur, I. Kweon, Rotation estimation and vanishing point extraction by omnidirectional vision in urban environment, *Int J Robot Res*, 31 (2012) 63-81.
- [8]" J. Liu, J. Yang, D. Dong, W. Zhou, Optoelectronic aiming and orientation system of laser tracker, *Optics and Precision Engineering*, 23 (2015) 1558-1564.
- [9]" J. Zhou, H.-J. Kang, A hybrid least-squares genetic algorithm-based algorithm for simultaneous identification of geometric and compliance errors in industrial robots, *Advances In Mechanical Engineering*, 7 (2015).

Improved Adaptive Median Filtering for Structured Light Image Denoising

Jialin Tang

Key Laboratory of Photoelectric Imaging Technology
and System, Ministry of Education of China, Beijing
Institute of Technology, Zhuhai
Zhuhai, China
e-mail: 01068@zhbit.com

Yuke Wang

Key Laboratory of Photoelectric Imaging Technology
and System, Ministry of Education of China, Beijing
Institute of Technology, Zhuhai
Zhuhai, China
e-mail: wangyuke94@163.com

Wei Cao

Key Laboratory of Photoelectric Imaging Technology
and System, Ministry of Education of China, Beijing
Institute of Technology, Zhuhai
Zhuhai, China
e-mail: 17303@bitzh.edu.cn

Juqing Yang

Key Laboratory of Photoelectric Imaging Technology
and System, Ministry of Education of China, Beijing
Institute of Technology, Zhuhai
Zhuhai, China
e-mail: yangjuqing@aoe.ac.cn

Abstract—In order to overcome the shortcomings of standard median filtering and adaptive median filtering in the denoising of structured light image, an improved adaptive median filtering method is proposed. The method determines the true noise point and the local noise density through two noise detections. Moreover, the size of the filtering window is selected according to the density, and the detected noise points are filtered by using the proposed method. The experimental results show that the improved adaptive median filtering can effectively protect the image details when noise is removed. And the proposed method can provide better filtering performance than standard median filtering and adaptive median filtering.

Keywords—adaptive median filter; noise detection; structured light image

I. INTRODUCTION

When acquiring a structured light stripe image, the disturbances including ambient illumination, possible optical diffraction, nonlinear distortion of the camera lens, reflected light from the surface of the object being measured, and noise pollution in the imaging process, will affect the quality of the acquired image severely, which may cause noise. The polluted structured light images make the subsequent processing harder, such as the extraction of feature information, three-dimensional reconstruction [1,2].

Median filtering has been widely used in image noise reduction. However, the denoising performance of standard median filtering is greatly affected by the size of the filtering details [3]. In addition, this method has certain contradictions in restraining the image noise and protecting details [4].

The small filtering window can protect details better in the image, however, the ability to denoise is limited. The large filtering window can enhance robustness against the noise, but the protection of details will be weakened [5,6].

In this paper, an improved adaptive median filter is proposed. The basic idea follows by two steps: Firstly, finding the existing noise, then select the size of the filter window adaptively according to the noise density. Secondly, the improved median filtering method is used to filter the noise. The improved adaptive median filter proposed in this paper greatly alleviates the contradiction between noise suppression and details protection. And the better filtering performance than the standard median filter and adaptive median filter can be provided.

II. IMPROVED ADAPTIVE MEDIAN FILTER

The proposed improved adaptive median filtering method includes three steps: (1) Detecting the noise of noised image twice; (2) Adjusting the size of the filtering window adaptively according to its local noise density; (3) Filtering the detected images from four given directions.

III. NOISE DETECTION OF THE ORIGINAL IMAGE

Noise detection is a key step in the filtering algorithm. The goal of this step is to find the true noise point in the image. A good noise detection method should try to avoid the possibility of error detection and false detection. Error detection is to define noise as a signal, which will affect the overall filtering effect; False detection is to define the signal as noise, and ultimately damage the image details [7,8]. Therefore, in order to detect noise more accurately, the detection noise can be divided into two steps: (1) The candidate noise point is determined; (2) The pseudo noise points are eliminated according to the formula.

A. Determining Candidate Noise Points

The size of the image I is $R * C$. The pixel value of pixel point p_{ij} is y_{ij} . The filter window size of $5 * 5$ was selected for the first noise detection. When p_{ij} is taken as

the central pixel point in the filtering window, then the set of all pixel values in this window Y_{ij} can be expressed as:

$$Y_{ij} = \{y_{i+w,j+h} \mid -2 \leq w \leq 2, -2 \leq h \leq 2, (i, j) \in I\} \quad (1)$$

In the set Y_{ij} , the maximum and minimum values of Y_{ij} are respectively recorded as y_{\max} , y_{\min} , if $y_{ij} = y_{\max}$ or $y_{ij} = y_{\min}$, the pixel p_{ij} is defined as the candidate noise point. The set f_{ij} is set as noise image and expressed as:

$$f_{ij} = \begin{cases} 1 & y_{ij} = y_{\max} \text{ or } y_{ij} = y_{\min} \\ 0 & \text{other} \end{cases} \quad (2)$$

B. Noise Detection

In an image, the pixel value of some signals may be very high or low. In the first step of detection, it is directly regarded as a noise point, causing misjudgment. In order to prevent such a situation, it is necessary to carry out the second step of noise detection.

Set D_{ij} as the set after removing the extreme points and expressed as:

$$D_{ij} = \{y_{i+w,j+h} \mid y_{i+w,j+h} \neq y_{\max} \text{ and } y_{i+w,j+h} \neq y_{\min}, y_{i+w,j+h} \in Y_{ij}\} \quad (3)$$

The average value of D_{ij} is expressed as:

$$M(D_{ij}) = \frac{1}{k} \sum_{y_{i+w,j+h} \in D_{ij}} y_{i+w,j+h} \quad (4)$$

The pixel value of the candidate noise point is compared with the average value. If the absolute value of their difference is larger than the threshold value, it indicates that the candidate noise point is the actual noise point. The formula below shows that:

$$f_{ij} = \begin{cases} f_{ij} \mid y_{ij} - M \mid > T \text{ and } f_{ij} \neq 0 \\ 0 & \text{other} \end{cases} \quad (5)$$

The threshold T has a great influence on the effect of noise detection and is defined as:

$$T = \sqrt{\frac{1}{k} \sum_{y_{i+w,j+h} \in D_{ij}} (y_{i+w,j+h} - M(D_{ij}))^2} \quad (6)$$

IV. SELECTION OF ADAPTIVE FILTERING WINDOW

In order to better suppress noise and save image detail information, local noise density should be introduced to

determine the size of filtering window. The expression of local noise density is:

$$R = \frac{\text{Number}_{\text{noise}}}{\text{width}_{\text{window}} \times \text{height}_{\text{window}}} \quad (7)$$

The local noise density is very small, and the size of filter window should also be relatively small, so as to ensure the de-noising effect and protect the details of the image. Conversely, the local density is large, so the size of the filter window should be larger, so as to maintain the ability of de-noising. According to this principle, the selection of the filter window size is adaptively determined by the density of each noise point. The size of the filter window l is defined as follows:

$$l = \begin{cases} 3, R \leq r_1 \\ 5, r_1 \leq R \leq r_2 \\ 7, R \geq r_2 \end{cases} \quad (8)$$

In the formula, r_1 and r_2 are constants, and their values are obtained according to experiments.

V. NOISE FILTERING

According to the above two steps, there are only two noise points left in the image: true noise points and non-noise points. Non-noise points do not need to be processed, and their own pixel gray values are directly preserved. The noise points need to be filtered. The method used in this paper is to select the pixel values of the pixels in the four specific directions in the filtering window, sequentially sort the pixel values, and weight the median obtained after the sorting [9]. Finally, the result obtained by the algorithm is substituted for the central value in the filtering window.

Assuming that the pixel value of $p(m, n)$ contaminated by noise is $f(m, n)$, then four specific directions in the filtering window are selected, which are 0° , 45° , 90° , 135° . Thus, four sub-windows can be obtained, which can be defined as:

$$\begin{cases} W_1(m, n) = \{f(m, n+l), -L \leq l \leq L\} \\ W_2(m, n) = \{f(m+l, n+l), -L \leq l \leq L\} \\ W_3(m, n) = \{f(m+l, n), -L \leq l \leq L\} \\ W_4(m, n) = \{f(m, n+l), -L \leq l \leq L\} \end{cases} \quad (9)$$

The size of the filter window is $(2L+1) \times (2L+1)$.

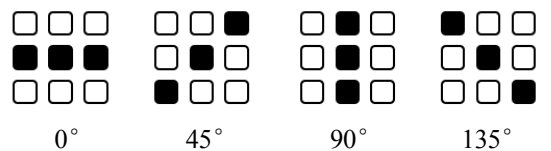


Figure 1. Four specific filtering direction.

$M_1(m, n)$, $M_2(m, n)$, $M_3(m, n)$ and $M_4(m, n)$ respectively represent the median values of pixels in the four sub-windows, namely:

$$M_k(m, n) = \text{med}[W_k(m, n)], k = 0, 1, 2, 3 \quad (10)$$

$\text{med}[\cdot]$ represents the median filtering. The above four sub-windows are respectively used to conduct median filtering for noise points. After filtering, the obtained value is:

$$g(m, n) = \sum_{k=1}^4 c_k M_k(m, n) \quad (11)$$

c_k is the weighted coefficient, and its value depends on the result of filtering in the above four directions, namely:

$$c_k = \frac{M_k(m, n)}{\sum_{k=1}^4 M_k(m, n)} \quad (12)$$

VI. EXPERIMENTAL RESULTS AND ANALYSE

A. Using the Lena Image

In this section, the Lena image is selected as the processing image. The proposed improved adaptive median filtering and traditional median filtering are compared by denoising ability and protecting detail ability under different degrees of noise interference. An objective evaluation was made using NMSE and PSNR as references. The formula for NMSE and PSNR is as follows:

$$NMSE = \frac{\sum_{i=0}^{255} \sum_{j=0}^{255} (g(i, j) - y(i, j))^2}{\sum_{i=0}^{255} \sum_{j=0}^{255} (y(i, j))^2} \quad (13)$$

$$PSNR = 10 \lg \frac{N^2 E^2}{\sum_{i=0}^{255} \sum_{j=0}^{255} (g(i, j) - y(i, j))^2} \quad (14)$$

$y(i, j)$ and $g(i, j)$ are the gray value of pixels in the image before and after denoising; E is the maximum value of $y(i, j)$; N is 256.

The results of denoising performance are analyzed by the standard median filters of 3x3, 5x5, adaptive and the proposed filter respectively based on the figure with the 4 different noise interference.

TABLE I. COMPARIDION OF PERFORMANCE PARAMETERS

Denoise Method	Parameters	Image Noise Level			
		1%	2%	5%	10%
3x3 med	NMSE	0.0000235	0.000047	0.000114	0.000226
	PSNR	25.34	22.34	18.49	15.51
5x5 med	NMSE	0.0000271	0.0000505	0.000118	0.00023
	PSNR	24.73	22.02	22.02	15.44

Denoise Method	Parameters	Image Noise Level			
		1%	2%	5%	10%
adaptive med	NMSE	0.0000238	0.000474	0.000115	0.00028
	PSNR	25.3	22.29	18.44	15.47
proposed method	NMSE	0.0000209	0.0000431	0.000105	0.00021
	PSNR	25.85	22.71	18.82	15.83



(a) Original Image; (b) Noise Image; (c) 3x3 Median Filtered Image; (d) 5x5 Median Filtered Image; (e) Adaptive Median Filtered Image; (f) proposed method Filtered Image;

Figure 2. Comparison of Lena.

From the results obtained in Figure 2 and Table 1, the NMSE value of the improved adaptive median filter in this paper is smaller than that of the 3x3 and 5x5 standard median filter and adaptive median filter, while its corresponding PSNR value is larger, which indicates that the improved median filtering is more capable of denoising and protecting details. The comparison was made by adding 2% noise interference: The standard median filtering of 3x3 has better performance in detail protection, but the image still contains partial noise; The standard median filtering of 5x5 can reduce the noise, but the image is fuzzy and the details are lost; The standard adaptive median filtering has both the advantages of 3x3 and 5x5 standard median filtering, the denoising ability is enhanced and the detail protection is improved. The improved median filter proposed in this paper filters out most of the noise, meanwhile the details in the image are relatively complete and the definition is relatively high.

The advantages of the improved median filter over the standard median filter can be explained as follows:

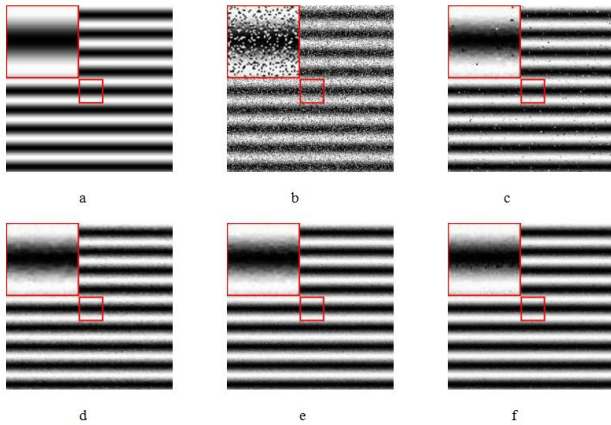
(1) The improved median filter first classifies the pixels in the image. And the pixels are divided into noise points and non-noise points. Then the image is filtered twice to remove the noise completely, while the pixel without noise pollution will not be filtered, and hence, the details are protected. The standard median filtering works for all pixels, which means those pixels without noise are also affected, making the image blurred and the details lost.

(2) The filter window size of the improved median filter is adaptively determined by the local noise density of the image, which combines both noise filtering and detail protection. The standard median filter uses the same filter

window size for the entire image, which has no adaptability and poor noise filtering effect. Compared with standard median filtering, the adaptive median filtering has improved noise filtering effect, but insufficient detail protection leads to image blurring.

B. Using Structured Light Image

Figure 3 (a) shows the initial structured light image, and Figure 3(f) shows the results after filtering using the improved algorithm. In terms of processing effect, the structured light strips processed by the new algorithm of this paper are clearer than the traditional methods, and the denoising effect is better.



(a) Original Image; (b) Noise Image; (c) 3x3 Median Filtered Image; (d) 5x5 Median Filtered Image; (e) Adaptive Median Filtered Image; (f) proposed method Filtered Image;

Figure 3. " Comparison of structural light image.

VII. CONCLUSION

In this paper, the improved adaptive median filtering uses a certain detection standard to detect the noise points in the image. The size of the filtering window adaptively adjusted according to the density of the detected noise points. And the detected noise points are filtered by using the proposed method. The proposed method greatly alleviates the

contradiction between noise suppression and details protection and has better filtering performance than the traditional median filter in the image preprocessing of structured light image.

ACKNOWLEDGMENT

This work is supported by the Science and Technology Service Network Initiative of the Chinese Academy of Sciences (Grant: KFJ-SW-STS-154), in part by the Research and Development Fund of Beijing Institute of Technology, Zhuhai (No. XK-2018-04, XK-2018-07 and XK-2019-01).

REFERENCES

- [1] Singh, Neeti, Thilagavathy, Thirusangu, Lakshmi Priya, Ramasubramanian T., et al. "Some studies on detection and filtering algorithms for the removal of random valued impulse noise." *IET image processing*, 2017, 11(11):953-963.
- [2] Zhongxin Gao. "An Adaptive Median Filtering of Salt and Pepper Noise based on Local Pixel Distribution." *the 2018 International Conference on Transportation & Logistics, Information & Communication, Smart City (TLICSC 2018)*.
- [3] Roy, Amarjit, Singha, Joyeeta, Manam, Lalit, et al. "Combination of adaptive vector median filter and weighted mean filter for removal of high-density impulse noise from colour images." *IET image processing*, 2017, 11(6):352-361.
- [4] Xiong, Hui Yuan, Y. Xu, and Z. J. Zong. "Accurate extrinsic calibration method of line structured-light sensor based on standard ball." *IEEE International Workshop on Imaging Systems & Techniques IEEE*, 2009.
- [5] Ataman, E., V. K. Aatre, and K. M. Wong. "Some statistical properties of median filters." *IEEE Transactions on Acoustics Speech & Signal Processing* 29.5(1981):1073-1075.
- [6] Gallagher, N., and G. Wise. "A theoretical analysis of the properties of median filters." *IEEE Transactions on Acoustics, Speech, and Signal Processing* 29.6(2003):1136-1141.
- [7] Jie Ping, Liu, and Y. U. Ying Lin. "A Flexible Method for Image Noise Removal." *Journal of South China University of Technology* (2000).
- [8] Xing, C. J., S. J. Wang, and H. J. Deng. "A new filtering algorithm based on extremum and median value." *Journal of Image & Graphics* (2001).
- [9] Wang, Jung Hua, and L. D. Lin. "Improved median filter using minmax algorithm for image processing." *Electronics Letters* 33.16(2002):1362-13

Underwater Image Enhancement Based on Stepwise Estimation of Transmission and Superpixel Segmentation

Yi-Ying Lu¹, Wei Cao¹, Jun-Wen Xue¹, Bing-Hua Su^{1,2}

¹Key Laboratory of Photoelectric Imaging Technology and System, Ministry of Education of China, Beijing Institute of Technology, Zhuhai
²Beijing Institute of Technology

Abstract—In order to solve the problem of detail loss and color cast caused by underwater imaging, we propose a novel underwater image enhancement method. We combine a stepwise estimate of transmission with a dark channel prior to obtain more detail from dark areas in underwater images. In addition, we use superpixel segmentation to avoid DCP invalid and white balance to correct color. The experimental results show that our method not only achieves a significant visual improvement, but also has a faster speed than other methods.

I. INTRODUCTION

The imaging process of the underwater images is similar to the haze images, as shown in Fig. 1. But the water in the ocean contains a variety of impurities, such that the light obtained by the imaging device is often subjected to physical processes of absorption and scattering[1]. However, for practical applications we need to get the true color of the object and as much detail as possible, especially in excavating underwater relics and carrying out the underwater rescue operations. Due to the discovery of more and more shipwrecks in recent years, underwater image enhancement technology has received more and more attention.

At present, most underwater image enhancement algorithms based on physical models are based on color channel and wavelength compensation[2,3]. In most cases, we used prior knowledge to estimate important parameters in the model and recover clear images through the inversion process[4]. But there are problems such as large assumptions and a priori knowledge limitation, at the same time, the color correction algorithm is not ideal[5].

In this paper a new enhance algorithm base on stepwise estimation of transmission, superpixel segmentation, DCP and guided filter was proposed. First, we split the image by superpixel segmentation to get the effective area for enhancing the images, at the same time we can get a bright area and a dark area of the image. For the dark area, we use dark channel prior to get the transmission and adaptive algorithm to correct the transmission from bright area. The experimental results show that the enhance effect of this algorithm is remarkable.

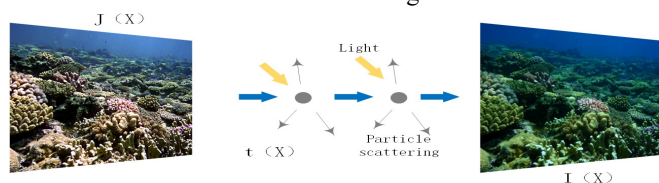


Fig. 1 Physical model of underwater imaging.

II. PROPOSED METHOD

In order to get accurate transmission and avoid DCP invalid we use superpixel segmentation to split the image into a visually significant irregular block of pixels consisting of adjacent pixels of brightness. The complex situation of underwater background light scattering and the calculation speed are considered comprehensively. We split the image into many blocks of similar brightness. The brightest area in the image, marked as a read block, is used as the effective area of background light. As shown in Fig. 2(a).

In particular, when the number of divided blocks of an image is two, the image is divided into a bright area and a dark area[6], as shown in Fig. 2(b). We must note that underwater the bright areas and the dark areas also represent the distance of the object were shooting from the camera. In most instances, the object closer to the camera is darker and the background seawater is brighter.

To avoid excessive enhancement of the image background water area, we use background light as a parameter of DCP algorithm to get the transmission of the dark area and obtain the bright area adaptively, as shown in Fig. 2(c).

Since the image is minimum filtered, many blocks will occur after the transmission is obtained, which will cause blurring of the edge area of the image after enhancement[7]. Therefore, we use guided filter to optimize the transmission, although it will reduce some accuracy but does not affect the enhancement effect, as shown in Fig. 2(d).

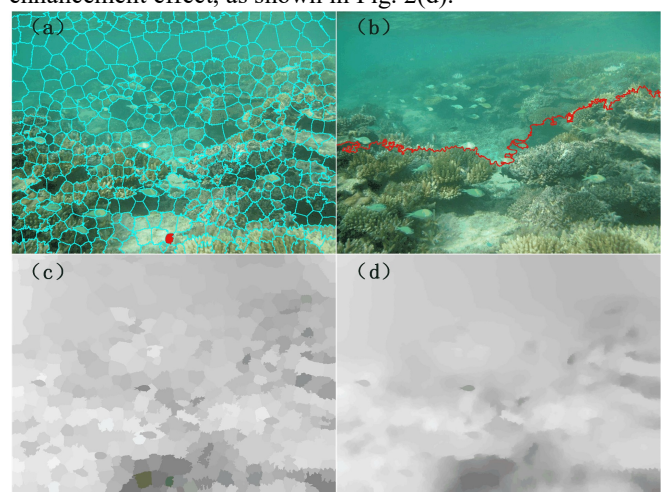


Fig. 2 (a) Background light image; (b) Bright and dark area image; (c) Transmission image; (d) Optimized transmission image.

III. EXPERIMENTAL RESULTS AND ANALYSIS

In order to verify the effectiveness of the algorithm, this paper selects four underwater color images with different degrees of blur. We compare the method in this paper with the Berman's method. The first column is the original image of the underwater, the second column is Berman's method[8,9], and third column is our method.

	Original Image	Berman's method	Our method
1			
2			
3			
4			

Fig. 3 Four experimental images and enhancement.

From the experimental results, it could be found that our method has a better effect on the restoration of image details than Berman's method. In the first row we can see that Berman's method lost texture of diver's clothes but our method enhance the details of the clothes. We also can see how the respirator looks like, as marked in Fig. 4.



Fig. 4 Marked images

In the second and fourth row, we can see that Berman's method overestimated the original color of the object, which caused the area overexpose and lost detail. But our method can clearly see the details of seaweed and fish, as marked in Fig. 5. Since there is a area where the brightness is significantly higher in the picture, the stepwise estimation of transmission has a significant effect. In the third row, our method retained the Layering of the object being photographed, and a small part of water in the bottom right corner was kept.



Fig. 5 Marked images.

The experiment is based on Windows 10 operating system, Matlab R2018a software platform, Intel(R) Core(TM) i7-6700HQ CPU @ 2.60 GHz 2.60 GHz, 16.0 GB memory hardware platform.

IV. CONCLUSION

A good transmission estimation method is very important for under water image enhancement. In this paper, a transmission estimation method, based on the improved stepwise estimation method is proposed which solved the problem of detail loss and color cast caused by variety of impurities.

This algorithm has wide applicability, and it can be applied to enhance multiple underwater conditions. A good detail and less color cast was just a part of underwater enhancement, next we should focus on how to restore the background color more beautiful.

ACKNOWLEDGMENT

This work is supported by Special Funds for the Cultivation of Guangdong College Students' Scientific and Technological Innovation. (NO.PDJHB0616) and grants from the Research and Development Fund of Beijing Institute of Technology, Zhuhai (No.XK-2018-04).

REFERENCE

- [1] L. Li, H. G. Wang and X. Liu, "Underwater Image Enhancement Based on Improved Dark Channel Prior and Color Correction," *Acta Optica Sinica*, 2017.
- [2] J. C. Guo, C. Y. Li, C. L. Guo, S. J. Chen, "Research progress of underwater image enhancement and restoration methods," *Journal of Image and Graphics*, 2017, pp. 273-287.
- [3] J. Y. Chian, and Y. C. Chen, "Underwater image enhancement by wavelength compensation and dehazing," *IEEE Transactions on Image Processing*, 2012, pp. 1756-1769.
- [4] Z. Q. Li, and J. S. Chen, "Supapixel Segmentation using Linear Spectral Clustering," *Conference on Computer Vision and Pattern Recognition*, 2015, pp. 1356-1363.
- [5] J. L. Tang, Z. B. Chen, B. H. Su, and J. F. Zheng, "Single Image Defogging based on Step Estimation of Transmissivity," *Chinese Conference on Image & Graphics Technologies*, 2017, pp. 74-84.
- [6] R. C. Gonzalez, R. E. Woods, and S. L. Eddins, "Digital Image Processing Using MATLAB," 2nd ed., 2009, pp. 1-827.
- [7] K. M. He, J. Sun, and X. O. Tang, "Guided image filtering," *IEEE Transactions on Pattern Analysis and Machine Intelligence*, 2013, pp. 1397-1409.
- [8] D. Berman, T. Treibitz, and S. Avidan, "Diving into Haze-Lines: Color Restoration of Underwater Images," *British Machine Vision Conference*, 2017.
- [9] D. Berman, T. Treibitz, and S. Avidan, "Non-local image dehazing," *Computer Vision and Pattern Recognition*, 2016.

编号: CSCY2020061604

EI 收录证明

委托单位: 北京理工大学珠海学院

委托人: 曹炜

检索数据库及年限: EI Compendex (1969-2020)

所检论文信息:

1. Underwater Image Enhancement Based on Stepwise Estimation of Transmission and Superpixel Segmentation

Lu, Yi-Ying (Key Laboratory of Photoelectric Imaging Technology and System, Ministry of Education of China, Beijing Institute of Technology, Zhuhai, China);

Cao, Wei; Xue, Jun-Wen; Su, Bing-Hua

Source: 2019 IEEE International Conference on Consumer Electronics - Taiwan, ICCE-TW 2019, May 2019, 2019 IEEE International Conference on Consumer Electronics - Taiwan, ICCE-TW 2019

Database: Compendex

Document type: Conference article (CA)

Accession number: 20201008256711

详情见附件, 特此证明 (检索日期: 2020年6月16日)。

检索人:  

审核盖章: 

广东工业大学图书馆

检索日期 2020年6月16日

AUTOMATIC ILLUMINATION SYSTEM FOR TOF CAMERA

Yujie Fang Binghua Su Xia Wang Xuedan Pei Su Yu Sufen Chen
Key Laboratory of Optoelectronic Imaging Technology and System, Ministry of Education,
School of Optics and Photonics, Beijing Institute of Technology, Beijing China
Beijing Institute of Technology, Zhuhai, Guangdong China

ABSTRACT

Attributed to the ability of three-dimensional scene direct acquisition in real-time, Time of flight (TOF) camera has been developed rapidly. Because of the problem of low resolution and accuracy, it are still difficult to be widely used. If these parameters can be further improved, TOF camera will win a place in the field of automatic navigation, machine vision and so on. In this paper, the imaging accuracy error caused by measuring distance and target reflectivity is analyzed. For the problem, that the weaker returned energy from the target is, the worse the imaging accuracy is, we proposed an automatic illumination system (AIS) which includes a distance weighted average metering (DWAM). It can solve the problem of imaging accuracy decline caused by the decrease of returned light energy and improve the dynamic performance of TOF camera.

INTRODUCTION

With the development of photon-detector technology, the TOF camera with the characters of cost efficiency, low power consumption and compact size has recently received significant attention and has great potential in the field of intelligent machine vision, human-computer interaction, indoor navigation and so on[1]. This is an active 3D imaging camera, which Optical sensors measure the delay between light emitted into a scene and received by a co-located sensor[2]. However, it is still not widely used because of its low resolution and poor measurement accuracy. In this paper, we found that the accuracy of TOF camera will be interfered by the imaging distance and reflectivity of objects which are metal, gypsum, plastic and other common materials[3]. The reason for this problem is an attenuation of returned light power from targets. So a kind of automatic illumination system (AIS) is proposed. Similar to common cameras, this system includes the part of light meter. In TOF camera system, the exposure time which is correlated to the depth resolution can not be changed arbitrarily. We do not talk about it. We focus on the compensation method of attenuation of returned light power at fixed frame rate and exposure time. Besides, a method DWAM is also proposed for the light meter part.

ERROR ANALYSIS OF TOF CAMERA

The TOF camera model we use is OPT8241CDK produced by TI for industry. Its basic imaging principle is that the phase difference between the modulated illumination and the returned light from targets is used to form depth map. Frame

rate is about 8-60fps. Each frame depth image is composed of n subframes and each of them are composed of m quads. The process of each quad on every pixel includes start-up, integral, readout and reset. So each frame of depth image needs mn quads which should be synchronized with illumination period. During every quads, sufficiently returned light power ensures the quality of the TOF imaging. This illumination period can be defined as exposure time of TOF camera. Fixed exposure time make the fixed frame rate. Based on this condition, we make some experiments with the materials of metal, gypsum, plastic, rough brick and smooth brick. The set of experiment is shown in Fig. 1. Made to parallel to sensors imaging plane, the surface of materials are image with TOF camera under different distances. No matter how far away from TOF sensor, the objects are imaged as full as field of view. We express the accuracy in standard deviation as follow:

$$STD = \sqrt{\frac{1}{N-1} \sum_{i=1}^{ab} |I_i - \mu|^2} \quad (1)$$

Where μ is the mean of I_i ,

$$\mu = \frac{1}{N} \sum_{i=1}^{ab} I_i \quad (2)$$

where ab is the product of sensor rows and columns.

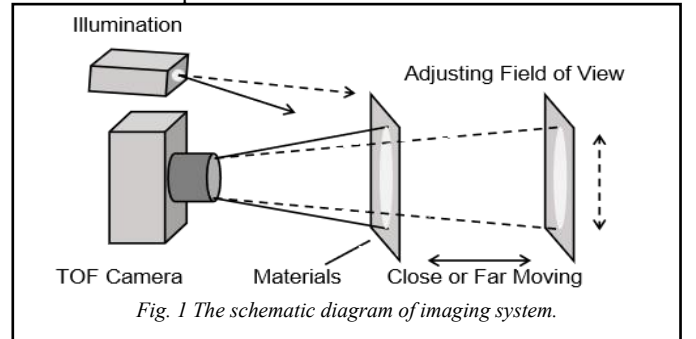
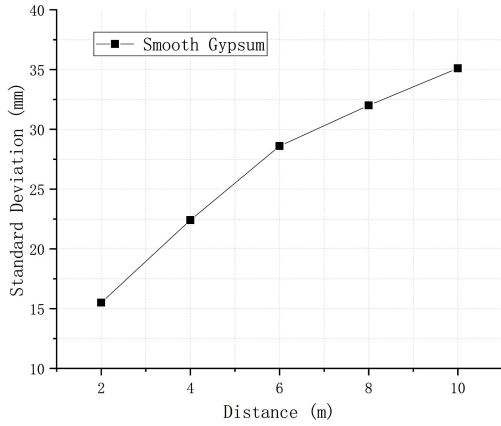


Fig. 1 The schematic diagram of imaging system.

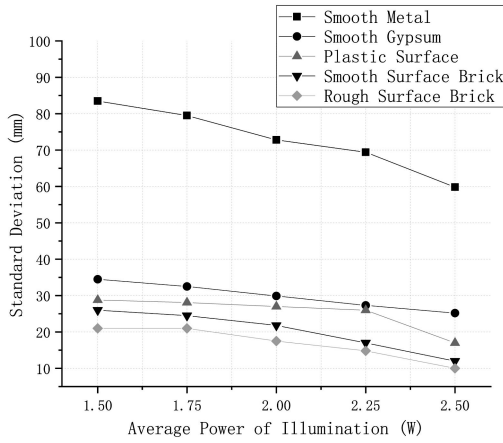
We make the scheme in experiment as follow: 1) Owing to the Lambert characteristic of gypsum surface, we image it in different distance. 2) Fixed imaging distance, different materials are imaged under different illumination power manually. As shown in Fig. 2.

AUTOMATIC ILLUMINATION SYSTEM

From the data, the more smooth and farther away the target is, the worse imaging accuracy will be. For this problem, an automatic illumination system (AIS) is propose. AIS is composed of controller algorithm and target light meter method. As shown in Fig. 3. The TOF camera OPT8241CDK uses four laser diodes (LD) as illumination. Their light power and working method can be easily controlled by software



(a) The standard deviation of smooth gypsum images at different distance.



(b) The standard deviation of materials images with different surface optical properties under different illumination power.
Fig. 2 The errors data of range maps collected under different condition.

through IIC bus on board. Whether to adjust the light power of LD depends on the results returned light from objects. The algorithm is proportional and integral (PI) structure which can make sure to control the LD driver quickly and accurately.

About the methods of light meter, TOF 3D camera is different from common color camera. The traditional methods include center weighted average metering, point-photometry and so on. Usually, the sensitivity of the camera sensor or exposure time is adjusted by judging the exposure of the images. These methods are not applicable to TOF cameras. In this work, distance weighted average metering (DWAM) is proposed. TOF camera can obtain the 3D information of target scene in real-time. Each pixel on the sensor can not only get the target distance value but also have the optical gray value. In general, people pay attention to the close-range scene, so the main idea of DWAM is that the weighted value of close scene is higher than that of far scene relatively. The compensation of light power will more inclined to the returned light energy of the target at close range. We can express it as:

$$P_l = \frac{1}{ab} \sum_{i=1}^{ab} w_i I_i \quad (3)$$

Where ab is the product of sensor rows and columns, and w_i is

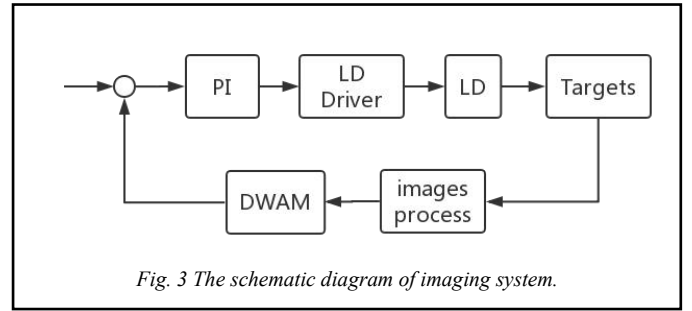


Fig. 3 The schematic diagram of imaging system.

the weighted value and I_i is the intensity on each pixel. P_l is result of light meter.

$$w_i = \frac{d_i}{S}, S = \sum_{i=1}^{ab} d_i \quad (4)$$

Where d_i is the depth value on each pixel.

This light meter method can ensure that the relatively close target has high priority to receive illumination compensation. However, this method is sensitive to noise, and a good clear image is an important prerequisite. In addition, some extreme cases are difficult to deal with. For example, there is an object with the similar character of mirror at a relatively far distance, which can strongly reflect signal light, while the relatively near interest objects has a low reflectivity. In such scene, some pixels may be saturated by strong reflection because of the illumination compensation of the near objects. This kind of problems can be studied by threshold partition, filtering, fuzzy recognition and so on in future.

CONCLUSION

In this work, we introduced an effective and simple method called automatic illumination system (AIS) that can solve the problem of accuracy decline which is produced by low power of returned light. And we also propose a light meter method that distance weighted average metering (DWAM) for TOF camera. Theoretically, the method can be used in various cases. However, in some extreme cases, such as very long imaging distance or extremely low reflectivity target, great illumination power is required. This problem should be optimized by engineering practices in next step.

ACKNOWLEDGEMENT

This work is funded by Beijing Institute of Technology, ZhuHai, grants XK-2018-01

REFERENCE

- [1] Luis Galarza, Harold Martin, Malek Adjouadi. "Time-of-Flight Sensor in a Book Reader System Design for Persons With Visual Impairment and Blindness," *IEEE Sensors Journal*, vol.18, pp.7697-7707, July, 2018.
- [2] Aniket Dashpute, Chandani Anand, Mukul Sarkar. "Depth Resolution Enhancement in Time-of-Flight Cameras Using Polarization State of the Reflected Light," *IEEE Transactions on Instrumentation and Measurement*, vol. 68, pp. 160-168, Jan. 2019.
- [3] Yujie Fang, Xia Wang, Yu Su, Kai Zhang, Binghua Su. "The Accuracy Analysis of TOF Camera Based on ANOVA," *2018 IEEE International Conference on Consumer Electronics-Taiwan*, Aug. 2018.

文献检索报告

委托人: 方宇杰

检索数据库:

1. EI《工程索引》

检索结果:

- 1、 EI《工程索引》收录论文 1 篇;
- 2、 其他详细信息请见附件。

检索日期: 2020 年 4 月 28 日

声明: 1. 本报告检索的文献信息均由委托人提供并确认, 如果由于委托人提供信息不实而造成任何后果, 本中心概不负责。

检索人 (签名):

湖南大学图书馆科技查新与文献检索中心

1. Automatic Illumination System for TOF Camera

Accession number: 20201008256992

Authors: Fang, Yujie (1, 2); Su, Binghua (1, 2); Wang, Xia (1, 2); Pei, Xuedan (2); Yu, Su (2); Chen, Sufen (2)

Author affiliation: (1) Key Laboratory of Optoelectronic Imaging Technology and System, Ministry of Education, School of Optics and Photonics, Beijing Institute of Technology, Beijing; 100081, China; (2) Beijing Institute of Technology, Zhuhai, Guangdong; 519085, China

Source title: 2019 IEEE International Conference on Consumer Electronics - Taiwan, ICCE-TW 2019

Abbreviated source title: IEEE Int. Conf. Consum. Electron. - Taiwan, ICCE-TW

Part number: 1 of 1

Issue title: 2019 IEEE International Conference on Consumer Electronics - Taiwan, ICCE-TW 2019

Issue date: May 2019

Publication year: 2019

Article number: 8991740

Language: English

ISBN-13: 9781728132792

Document type: Conference article (CA)

Conference name: 6th IEEE International Conference on Consumer Electronics - Taiwan, ICCE-TW 2019

Conference date: May 20, 2019 - May 22, 2019

Conference location: Address: No. 77, Jiankang Rd., Jiaosi Township, Yilan, Taiwan

Conference code: 157711

Publisher: Institute of Electrical and Electronics Engineers Inc.

Abstract: Attributed to the ability of three-dimensional scene direct acquisition in real-time, Time of flight (TOF) camera has been developed rapidly. Several products are already active in the consumer electronics market. Such as Mesa Imaging SwissRangers SR4500 and Microsofts Kinect V2. Because of the problem of low resolution and accuracy, all of them are still difficult to be widely used. If these parameters can be further improved, TOF camera will win a place in the field of automatic navigation, machine vision and so on. In this paper, the imaging accuracy error caused by measuring distance and target reflectivity is analyzed. For the problem, that the weaker returned energy from the target is, the worse the imaging accuracy is, we proposed an automatic illumination system (AIS) which includes a distance weighted average metering (DWAM). It can solve the problem of imaging accuracy decline caused by the decrease of returned light energy and improve the dynamic performance of TOF camera. © 2019 IEEE.

Number of references: 3

Main heading: Cameras

Uncontrolled terms: Automatic navigation - Consumer electronics markets - Distance weighted average - Dynamic performance - Illumination system - Measuring distances - Three-dimensional scenes - Time of flight (ToF) cameras

Classification code: 742.2 Photographic Equipment

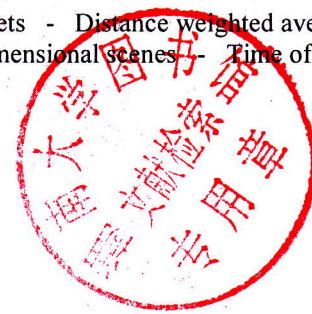
DOI: 10.1109/ICCE-TW46550.2019.8991740

Compendex references: YES

Database: Compendex

Compilation and indexing terms, Copyright 2020 Elsevier Inc.

Data Provider: Engineering Village



基于 ZigBee 和 Android 的古建筑火灾监测系统设计

黄娟¹, 程浩东², 李勇峰¹, 梁钦策²

(1. 北京理工大学珠海学院 信息学院, 广东 珠海 519085; 2. 西藏大学 工学院, 西藏 拉萨 850000)

摘要:针对西藏古建筑火灾复杂、可预测性差的特点,结合 ZigBee 与 Android 平台设计智能移动监测系统。该系统完成了 ZigBee 无线传感器网络设计、Android 客户端开发以及相关中间件的实现,各类传感器采集的数据通过 GPRS 上传至客户端。实验表明,该系统可以实现对古建筑环境信息的实时反馈和对用户指令的及时响应。

关键词:古建筑;火灾监测;ZigBee;Android;GPRS

中图分类号:X924.4, TN92 **文献标志码:**A

文章编号:1009-0029(2019)07-0973-04

西藏古建筑多采用土木、砖木等作为建筑材料,燃点较低,室内油灯常年点燃,烟火常年存在、消防基础设施薄弱、僧人及信教群众的消防安全意识不强等问题较为突出,藏区古建筑群建设的聚集程度较高,许多寺庙内还陈列着古代遗留下来的壁画、雕塑和其他文物,一旦引发火灾,将带来巨大损失。因此,设计一款火灾监测系统对生命财产安全具有重要意义。

有线连接对古建筑也有一定的损害,破坏整个建筑内部的整体美观,且一定时间线路将会老化,日常维护也很困难,可扩展性差,所以笔者使用了无线连接方式。无线传感器网络具有数据采集、无线通信、信息处理及协同工作等功能,可广泛应用于环境监测、工业控制、智能家居、抢险救灾、火灾监测报警和远程监测等。而 Android 具有人机界面友好、操作简单、安全性高等优点。笔者结合 ZigBee 和 Android 技术设计了基于无线传感器网络的古建筑火灾监测系统,可以对建筑进行全方位多角度的实时监测。

1 系统架构

该系统由信息采集层、数据处理层、传输层和应用层组成,其整体框架图如图 1 所示。信息采集层通过传感器网络采集环境参数,如 CO、烟雾浓度、温度、火焰等,并进行初级处理。

在数据处理层中,ZigBee 协调器汇聚所有节点发送的数据,并通过串口转发信息给嵌入式平台,平台显示本地信息并应用多数据融合技术综合处理建筑中的多个传感器的数据信息并封装。

传输层接收来自数据处理层的参数信息并使用 GPRS 网络上传至应用层。

应用层由服务器和 Android 软件应用组成。当传输

层传输数据到应用层的服务器中,服务器会将该数据信息转发至 Android 客户端。用户可以通过 APP 界面监视建筑内状态,获取古建筑环境信息,并发送控制指令信息。



图 1 系统框架图

2 硬件设计

本项目中的嵌入式平台主要有两个作用:一是用于接收 ZigBee 传输过来的信息并将之通过 GPRS 模块转发至服务器;二是接收并分析服务器的指令信息从而控制相应的节点设备。

嵌入式平台主要汇聚各个 ZigBee 节点的传感器信息并且通过广播发送指令信息控制 ZigBee 节点的工作。由于平台需要处理大量传感器数据,加之要求其具有高性能、低成本、低功耗等特点,适用于智能控制、警报系统等应用场合。因此,笔者采用 STM32F103ZET6 微控制器作为中心处理器。图 2 为嵌入式平台硬件设计原理图。



图 2 嵌入式平台硬件设计原理图

平台主要负责采集各节点的传感器信息,对数据信息进行处理、封装,包含显示电路、GPRS 电路。显示屏主要负责实时显示本地连接情况、环境信息,便于管理员管理维护本地设备。GPRS 电路为管理员远程监控建筑环境提供通信链路。

3 网络设计

3.1 无线传感器网络设计

在无线模块组成的网络中,一个无线模块即被称为一

个节点。

根据系统设计的需要,笔者通过协调器节点、路由节点、终端节点组成树状的网络结构,其拓扑图如图3所示。

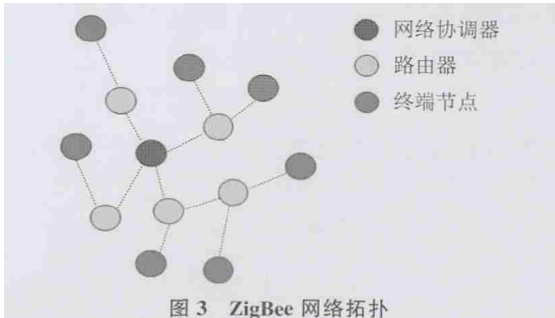


图3 ZigBee网络拓扑

树状网络非常适合监控相对较大的区域,节点通过协调器节点或者父节点接入网络,一个树状网络可以看成由一个协调器节点和若干个星形网络组成,一个星形网络覆盖一个小的区域,其内的节点将采集的信息通过父节点(路由节点)转发给协调器节点。每个节点只能和他的父节点和子节点之间通信,距离较远的路由节点也可以通过其附近的路由节点转发给协调器节点,通过一系列的转发,可以生成多个层级,网络还具备自组织、自愈功能。

3.2 系统网络设计

每个 ZigBee 节点与传感器组相连,通过电池供电,并且具有无线通信、简单的信息处理和预警等功能。节点将获取到的信息数据通过协调器反馈给嵌入式平台,嵌入式平台将处理后的数据通过 GPRS 上传至服务器。其整体结构图如图4所示。

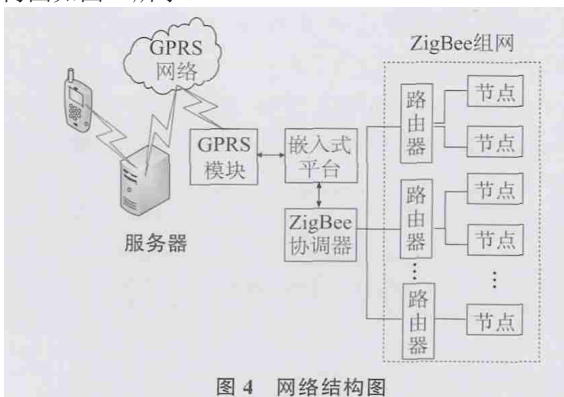


图4 网络结构图

4 系统软件程序设计

本系统软件程序涉及到 Android 客户端程序、服务器程序、STM32 嵌入式平台应用程序、ZigBee 数据收发程序等。限于文章篇幅,笔者只介绍 Android 客户端程序和 STM32 嵌入式平台应用程序。

4.1 Android 客户端程序设计

本系统中基于 eclipse4.3 软件开发 Android,网络通信协议选用 TCP/IP 协议。通过 IP 地址和端口号与服务器相连。其核心代码为:

```
s = new Socket("221.13.83.14", 30003);  
br=new BufferedReader(new InputStreamReader(  
s.getInputStream()));
```

```
os = s.getOutputStream();
```

应当注意的是,Android 联网需要相应的权限,代码如下:

```
<uses-permission  
android:name="android.permission.INTERNET" />  
<uses-permission  
android:name="android.permission.CHANGE-  
NETWORK_STATE"/>
```

前者为普通联网权限,后者为 WiFi 权限。

客户端通过 io 流操作逐行读取来自服务器的消息,用户可通过 APP 界面查看这些信息并发送相应指令。图5为 Android 客户端流程图。

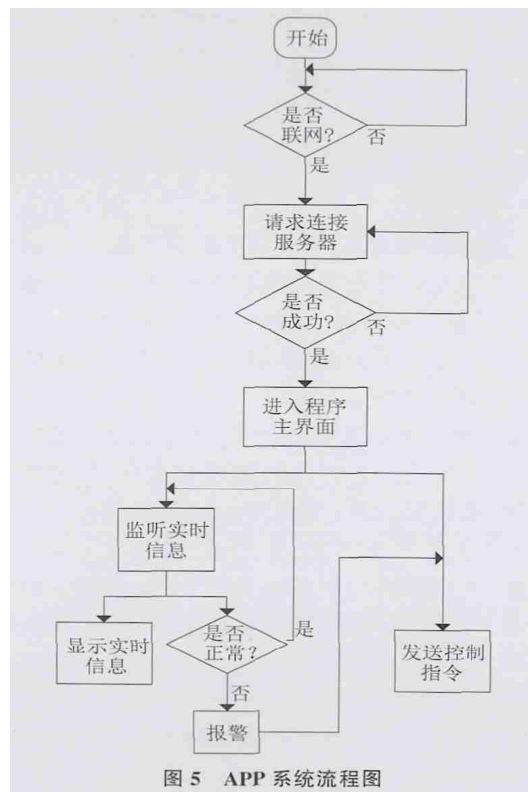


图5 APP系统流程图

4.2 硬件平台程序设计

4.2.1 STM32 数据传输

本系统中,笔者使用 C 语言对嵌入式系统进行编程,主要实现的功能就是通过 GPRS 发送传感器采集的数据至服务器和判断服务器发送过来的指令控制相应的设备。STM32 接收 ZigBee 协调器发送的数据和向 GPRS 发送数据都是通过串口交换数据的,为了便于数据解码,在数据传输中统一使用 UTF-8 编码方式。

4.2.2 ZigBee 无线通信协议

ZigBee 无线通信协议是用于数据在节点之间的传递。STM32 系统通过串口直接与 ZigBee 协调器交互,ZigBee 协调器与 ZigBee 节点之间采用的是无线通信,因此设计了查询、控制节点等报文。协调器通过发送报文获取节点信息及控制节点,表1为查询所有终端数据发送报

文格式,其共有 6 Byte,由开始码、地址、功能码、校验码和结束码组成。功能码表示命令的类型,地址代表某个节点的身份,2 Byte 的网络开发地址。因数据传输采用打包机制,故查询数据时只需查询所有终端上所有传感器的数据即可,从而节省网络带宽。

表 1 查询终端数据发送报文格式

开始	地址	功能码	校验码	结束
1 Byte	2 Byte	1 Byte	1 Byte	1 Byte

ZigBee 协调器与 ZigBee 节点之间采用的是无线通信,因此设计了一种可扩展的无线数据响应报文格式,如表 2 所示,总体分为五部分,即:开始码、执行状态、数据、校验码和结束码。数据即采集到的传感数据,数据根据节点数量扩展的数据空间。表 3 中,单个节点数据为 2 Byte 的空气温湿度、2 Byte 的 CO 浓度、2 Byte 的烟雾浓度数据以及 1 Byte 火焰强度。表 4 为控制终端的协调器向终端节点发送的控制报文。

表 2 终端响应报文格式

开始	地址	功能码	数据	校验码	结束
1 Byte	2 Byte	1 Byte	1 Byte	1 Byte	1 Byte

表 3 终端响应报文中单个节点数据内容

命令头	...	第 n 个节点数据				...	命令尾
		温湿度	CO 浓度	烟雾浓度	火焰强度		
		2 Byte	2 Byte	2 Byte	1 Byte		

表 4 控制终端发送报文格式

开始	执行状态	数据	校验码	结束
1 Byte	1 Byte	...	1 Byte	1 Byte

5 测试与分析

系统搭建结束,对其进行测试,选用 OPPO R7 手机作为测试机。将 APP 安装好之后,打开服务器等待连接,APP 和嵌入式平台通过 IP 地址和端口号与服务器建立连接。笔者在西藏大学工学院 1 号实验楼 407 室设置若干 ZigBee 节点进行模拟实验。以实验室模拟古建筑环境,并通过燃放易燃物等操作模拟建筑内环境,并通过 ZigBee 节点获取环境信息。

首先通过手机发送指令,获取整个传感器网络节点的实时数据,通过 APP 顶部下拉框可监测不同节点的实时信息。当点击刷新数据按钮时,APP 会发送对应指令至服务器,APP 通过服务器反馈的信息判断指令是否发送成功,并通过屏幕中间的 TextView 文本框提醒用户,同时更新各项参数数据,APP 会周期地获取数据,并根据人为设定的临界值自行判断环境参数是否正常,并提示用户。

APP 根据各个节点信息判断建筑内环境参数有可能发生火灾时,会发出警报。系统通过判断温度、湿度、CO、烟雾 4 个参数中的某个参数是否超过临界值,智能选择灭

火方式;若系统出现故障,用户亦可通过 APP 手动警报,APP 会通过服务器将指令发送至嵌入式平台,嵌入式平台接收到警报指令,扬声器会发出警报提示寺庙的工作人员和游客,并人为完成控制寺庙中的设备选择浇水灭火或干粉灭火等操作。再次点击按钮,即可停止警报。

经过实验测试,APP 可以获得较为准确的建筑实时信息数据,同时嵌入式平台能及时响应用户的指令并进行相应的操作。因此,该系统能较好地应用于寺庙等环境复杂的场景,并能提供较高的安全保障,实用性较强。

6 结束语

西藏古建筑火灾监测系统将 ZigBee 无线传感器网络技术和 Android 技术整合到一起,实现了对古建筑的温湿度、CO、烟雾浓度、火焰强度等环境信息的实时监测和整体防护。经实验验证,该系统可以准确地监测古建筑环境信息与判别安全参数,并能及时响应 APP 端的控制指令,系统使用方便、性能稳定,适合古建筑等环境参数复杂的环境使用。

参考文献:

- [1]陶佳峰,杨晓洪,王剑平,等.基于 ZigBee 和 STM32 的实验室无线远程管理系统[J].价值工程,2016,35(4):56-59.
- [2]朱晋梅.基于无线传感器网络的牵引数据采集与传输系统的研究[D].成都:西南交通大学,2012.
- [3]许秀富,吕小南.Android 手机的智能家居语音控制系统设计[J].单片机与嵌入式系统应用,2018,18(1):48-51+56.
- [4]郭少敏,石军锋.基于 Android 和 ZigBee 的嵌入式 Web 服务器设计[J].现代电子技术,2018,41(8):100-103.
- [5]庞娜.网状结构 ZigBee 无线传感器网络研究[D].长春:吉林大学,2010.
- [6]晏均,群彪,晓阳.基于无线传感器网络的室内火灾报警系统[J].中国民航飞行学院学报,2009,(2):45-48.
- [7]李勇峰,高杨,黄娟,等.模糊神经网络算法在藏区古建筑火灾探测中的应用[J].消防科学与技术,2015,34(12):1625-1628.
- [8]徐文.基于 WiFi 与 Android 的智能家居监控系统设计[D].成都:西南交通大学,2017.
- [9]卜令冰.基于 ZigBee 技术的智能楼宇防火监控系统的设计[D].淮安:安徽理工大学,2016.
- [10]李勇峰,闫星位,黄娟,等.基于 Android 的藏汉双语大棚远程监控系统的设计与实现[J].电视技术,2017,41(11/12):198-202.

Design of ZigBee and Android based fire monitoring system for ancient buildings

HUANG Juan¹, CHENG Hao-dong²,
LI Yong-feng¹, LIANG Qin-ce²

(1.School of Information Technology, Beijing Institute of Technology, Zhuhai, Guangdong Zhuhai 519085, China; 2.School of Engineering, Tibet University, Tibet Lhasa 850000, China)

Abstract: Aiming at the complex fire situation and poor predictability-

ty of ancient buildings in Tibet, an intelligent mobile monitoring system was designed based on ZigBee and Android platform. The system completes the design of ZigBee wireless sensor network, the development of Android client and the implementation of related middleware. The data collected by various sensors is uploaded to the client through GPRS. Experiments show that the system can realize real-time feedback of ancient building environment information and timely response to user instructions.

Key words: ancient building; fire monitoring; ZigBee; Android; GPRS

作者简介:黄娟(1982-),女,湖南沅江人,北京理工大学珠海学院信息学院副教授,硕士,主要从事计算机科学方面的教学工作,广东省珠海市金凤路6号,519085。

通信作者:李勇峰(1980-),男,北京理工大学珠海学院信息学院副教授。

收稿日期:2019-02-26

(上接第972页)

通过锥形水雾上方空隙蔓延出火源区域,且随着燃烧的不断进行烟气体量越来越多,有少部分烟气由下端蔓延出隧道,说明细水雾在火灾前期有良好的阻隔烟气的作用,但随着燃烧的持续进行,阻烟效果会降低。

(2)细水雾具有良好的隔热降温效果。无细水雾作用时,隧道内都处于较高温度,尤其是顶棚附近烟气温度较高,对隧道内人员生命安全和隧道结构的稳定程度构成很大危险。细水雾开启后,火场内温度有明显降低,对顶棚温度的降低效果良好,很好地保护了隧道刚性结构。

(3)起火点不同位置对细水雾性能无明显影响,烟气的蔓延规律基本一致。火源位于侧壁时细水雾的降温效果相较于地面中心较小,但对不同功率火源均有明显降温效果,降温效率稳定。

(4)细水雾系统应用于实际工程中时,可通过调节喷头压力改变细水雾的雾滴粒径,喷头压力越大,雾滴粒径越小,吸热蒸发速率越快,对火场热量隔绝能力越强,降温隔热效果越好。但喷头压力对管网设计要求较高,且细水雾降温效果并非一直随喷头压力增大而更好,应根据实际管网设计、水量要求等情况合理选择喷头压力。

参考文献:

- [1] 朱伟. 狭长空间纵向通风条件下细水雾抑制火灾的模拟研究[D]. 合肥:中国科学技术大学,2006.
- [2] 李梦. 细水雾技术在隧道中应用的实验与数值模拟研究[D]. 合肥:中国科学技术大学,2016.
- [3] 吕浩宇,李椿,董海涛,等. Hall效应对三维磁流体发生器的影响[J]. 力学学报,2008,(3):306-314.
- [4] 李涛,谢玮,苏紫敏,等. 受限空间水幕隔热阻烟性能的试验研究[J].

· 科技信息 ·

火灾中钢材热-力耦合分析材料模型研究

英国研究人员开展了火灾中钢材热-力耦合分析材料模型的研究。建立了高温下钢结构多轴应力分析的新材料模型。研究提出的各向同性-动态硬化材料组合模型,考虑了包兴格效应、瞬态硬化行为、地震后引发的火灾以及火灾蔓延造成的多轴结构分析时的荷载变向。所提出的材料模型已在 ABAQUS 中使用 UMAT 子程序实现,并与实验数据进行了验证,取得了较好的一致性。该模型在分析经受实际建筑火灾的结构受力性能方面也开展了应用,适用于基于性能化的工程结构火灾分析。

肖科 供稿

中国安全生产科学技术,2016,(12):154-159.

[5] 田向亮. 细水雾与火灾相互作用的研究[D]. 沈阳:东北大学,2014.

Fire control performance of water mist system in urban highway tunnel

SU Zi-min, HUANG Bao, FENG Jian-an

(Nanning Rail Transit Co., Ltd, Guangxi Nanning 530029, China)

Abstract: A tunnel model was established, fire scenarios was set by changing parameters such as power of fire source, position of fire source, number of water mist nozzles and diameter of mist droplets, to study the fire control performance of water mist in urban highway tunnel. The research results showed that the water mist has good cooling and heat insulation effect, which can prevent the smoke diffusion better. When the fire source is close to the tunnel sidewall, the cooling effect is slightly worse than when the fire source is located at the center of the tunnel ground. The larger the nozzle pressure, the smaller the spray particle size, the larger the contact surface with the flue gas, the higher the heat absorption and evaporation efficiency, and the better the cooling effect.

Key words: tunnel fire; water mist; numerical simulation; smoke spread; cooling efficiency

作者简介:苏紫敏(1995-),女,广西南宁人,南宁轨道交通集团有限责任公司助理工程师,学士,主要从事地铁消防技术管理,广西壮族自治区南宁市青秀区云景路83号,530029。

收稿日期:2019-02-26

计及激励型需求响应的电动汽车聚合商充电优化调度

官鑫, 苏禹, 张小凤, 黄相杰

(北京理工大学珠海学院 信息学院, 广东珠海 519085)

Optimal Charging Scheduling for Electric Vehicle Aggregator Considering Incentive Demand Response

GONG Xin, SU Yu, ZHANG Xiaofeng, HUANG Xiangjie

(School of Information, Zhuhai Campus of Beijing Institute of Technology, Zhuhai 519085, China)

摘要: 研究了电动汽车聚合商如何决策最优的经济激励值和充电量, 以达到收益最大化的目的。提出了用户向聚合商交流其充电情况的主动需求响应方式; 构造了基于经济激励的电动汽车聚合商的最优充电调度模型, 所建立的调度模型是一个二层模型, 上层以聚合商收益最大为目标, 以用户主动需求响应量为约束, 下层为实时电力市场的出清模型, 上层模型中的市场电价来自于下层模型; 将该模型转化为混合整数线性规划模型, 采用拉格朗日替代法与分支切割法的协同组合方法求解。算例分析表明所提模型能够提高聚合商的收益。

关键词: 电动汽车聚合商; 激励型主动需求响应; 充电调度; 电力市场; 电动出租车

Abstract: An active demand response approach was proposed for electric vehicle users by reporting their charging status to the aggregator. Optimal charging scheduling model of the aggregator in the real-time electricity market considering coupon-based active demand response was built. This bi-level model was constructed with the upper level model aiming at maximizing the aggregator's revenue constrained the consumer's active demand response, and the lower level market clearing model providing market price for the upper model. The optimal charging scheduling model is a mixed integer linear programming model solved by the combination of Surrogate Lagrangian Relaxation and Branch-And-Cut method. The example analysis shows that the proposed model can increase the aggregator's profit.

Keywords: electric vehicle aggregator; incentive active demand response; charging schedule; electricity market; electric taxi

基金项目: 广东省普通高校特色创新项目 (2015KTSCX173); 北京理工大学珠海学院校级科研项目 (XK-2018-25)

0 引言

大量电动汽车接入电网充电会对电网产生重要影响, 为有效降低其负面影响, 已有较多有序充电方面的研究成果发表, 主要可归结为直接充电负荷控制方法和电价引导方法^[1]。电价引导有静态分时电价和动态分时电价。静态分时电价其费率 and 时段固定, 简单易行, 但可能导致系统负荷在夜间出现另外一个高峰, 影响配网的安全运行。为解决这一问题, 有研究者提出了动态分时电价, 调度机构在有新的电动汽车入网时重新计算新的分时电价时段, 但由于电动汽车不是同时接入电网, 每当有电动汽车入网就要计算一次, 计算量大。因此, 当电动汽车数量达到一定规模后, 无论是直接控制充电负荷还是用电价引导, 由调度机构统一管理每辆电动汽车是不现实的。比较可行的方案是通过聚合商, 对电动汽车实行分散管理。我国新电改提出了放开售电侧市场, 允许不同的市场主体组建售电公司^[2-3]。电动汽车聚合商属于售电公司的一种, 从批发市场购电再出售给电动汽车用户。作为一个追求利润的独立售电公司, 聚合商的目的是最大限度地提高收益, 因此, 聚合商利益的优化是一个重要的问题。

随着电动汽车的发展, 电动汽车不仅在私家车中占有很高比例, 以出租车为代表的公共交通工具也将逐步被电动汽车取代^[4]。与私家车相比, 出租车每天需要保持更长时间地运行状态, 需要消耗更多的电量, 用电特性也更加复杂^[5-8]。本文研究的前提是聚合商旗下有私家车和出租车 2 种用户, 由于电动汽车行为的随机性, 聚合商从现货市场购电

以满足用户的充电需求。聚合商会在日前市场购买一部分电能，但是到了实际时刻，用户的充电需求可能会和日前购买量有所差别，尤其是出租车，其接入电网的随机性较大，日前市场购买的电能可能与实际需求相差较大，因此需要进一步在实时市场进行交易。聚合商在实时市场购电时，需要确定购电量，这使得开展电动汽车聚合商充电调度的研究具有重要意义。

目前已有少数文献研究了电动汽车聚合商在日前市场如何确定最优的充电量^[9-20]，但文献中的电动汽车用户均为私家车，没有考虑电动出租车，而且也没有考虑需求响应。实时市场的批发电价是波动的，而如果聚合商对用户的零售电价固定，这会给聚合商带来一定的利润风险，此时聚合商可以通过向用户提供需求响应项目来降低损失。通过需求侧响应，一方面，用户可以通过响应聚合商的负荷调节信号来获得补贴；另一方面，聚合商可以利用需求侧的弹性在电力市场中选择更有利的报价策略，进而降低购电成本和运营风险，增加收益^[21]。

需求响应通常分为价格型需求响应和激励型需求响应。价格需求响应下，用户被迫接受随批发电价波动而变化的零售电价，在用户接受度和公平性方面存在问题。激励型需求响应中应用比较广泛的是可中断负荷，但有研究表明由于该项目强制中断用户用电，给用户的生活带来不便，可能会引起用户的反感^[22]。

为此，本文设计了基于经济激励的需求响应方式鼓励用户减少负荷。与可中断负荷方式相比，本文的需求响应方式是建立在用户自愿响应的基础上，用户有权选择是否参与响应，参与意愿度更高。与价格型需求响应相比，用户面对的是固定的零售电价，更易于接受，其实施背景与现有的固定零售电价模式一致，更容易实施。

有文献研究了普通负荷聚合商如何利用奖励券激励用户减少负荷，其计算奖励券的方法有 2 种：一是聚合商向用户公布奖励券，用户反馈给聚合商其用电量，聚合商重新计算奖励券并再次公布，如此迭代多次直到收敛^[22]，花费时间较长；二是聚合商在发放奖励券之前先估计用户的响应^[21]，然而不同的估计方法导致不同的结果。2 种方法其本质均为被动需求响应，本文采用用户通过与聚合商交流其放弃充电所要求的经济激励值来参与需求响应的主动需求响应方式，聚合商和用户之间迭代一

次即可。

本文首先介绍了电动汽车聚合商的购电过程；接着给出了实时市场出清模型；然后分析了电动汽车充电负荷与经济激励的关系，提出了计及激励型主动需求响应的聚合商在实时电力市场的最优充电调度模型；最后将模型转化为混合整数线性规划模型，采用拉格朗日替代法与分支切割法的协同组合方法求解，并通过算例对方法的有效性进行了验证和分析。

1 聚合商的最优充电调度模型

1.1 聚合商的购电过程

电力市场结构如图 1 所示。发电商向交易中心提交报价，聚合商向交易中心提交购电量，交易中心进行市场出清确定市场电价和交易量。

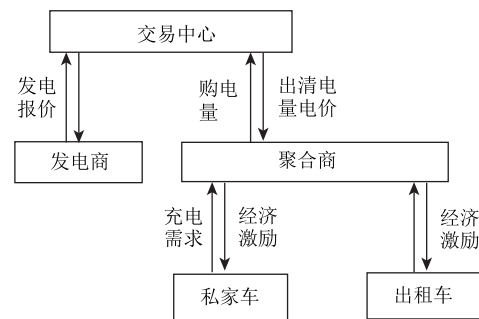


图 1 电力市场结构图

Fig. 1 Structure of the electricity market

每个时刻前 15 min，在该时刻想要充电的私家车和出租车用户告知聚合商其充电需求。电网公布该时刻的系统条件或者天气情况的重大变化，聚合商结合历史报价和负荷数据，模拟实时市场出清过程计算实时批发电价。聚合商通知有充电需求的用户提交放弃充电所要求的经济激励值，然后综合各个用户上传的数据得到总的“经济激励值—用电量”曲线，通过优化计算确定经济激励值和最终的充电量，最后向用户发放经济激励，向电力市场交易中心提交购电量。

1.2 实时市场出清模型

设在实时电力市场中，交易中心采用统一电价出清，市场出清模型的目标为发电商成本最低，决策变量为市场电价和各发电商的发电量，即通过求解以下模型进行出清：

目标函数为

$$\min \sum_{i=1}^N c_i q_i \quad (1)$$

约束条件为

$$\sum_{i=1}^N q_i = x_t + D_t : \lambda_t, \quad \forall t \quad (2)$$

$$q_{i\min} \leq q_i \leq q_{i\max} : \omega_{i\min}, \omega_{i\max}, \quad \forall t \quad (3)$$

式中: N 为发电商的数量; c_i 为发电商 i 在 t 时刻的报价参数; q_i 为发电商 i 在 t 时刻的发电量; x_t 为聚合商在实时市场的购电量; D_t 为其他实时平衡负荷; $q_{i\min}$ 和 $q_{i\max}$ 分别为发电商 t 时刻发电量的最小值和最大值; λ_t 为实时市场的出清电价; $\omega_{i\min}$ 和 $\omega_{i\max}$ 分别为约束条件(3)对应的拉格朗日乘子。

1.3 电动汽车充电负荷与经济激励的关系

根据私家车用户对激励的响应方式不同, 将私家车用户分为以下 2 类。

第 1 类用户: 出行时间距离当前时间很紧, 剩余电池容量较少, 需要立刻充电, 则该类用户不响应经济激励。

第 2 类用户: 出行时间距离当前时间较长, 是否响应激励与其收入水平有关。不同收入水平的用户, 对接受激励后电费支出减少率的响应不同, 这里采用用户向聚合商上报其所要求的激励值的方式, 各用户计算出使其电费减少率达到自己期望的激励值并上报给聚合商, 即通过式(4)计算激励值。

$$\frac{C_0 - A_j P_j}{C_0} = B \quad (4)$$

式中: C_0 为不响应激励时用户的电费; A_j 为用户 j 上报的激励值; P_j 为用户 j 的充电功率; B 为期望的电费减少率。

出租车用户向聚合商上报的数据为其 t 时刻不充电所要求的经济激励, 其计算原理如下:

出租车电池的电量是有限的, 对于任意时刻的某一剩余电量, 可以计算出出租车的可运营时间 T 和可充电时段。为使出租车保持运营状态, 在可运营时间内至少选择 1 个时段充电^[22]。例如, 假设电动出租车的电池余量为 10% 时可运营 1 个时段。为减少电池损耗, 设在剩余电量为 20% 时, 必须充电。则在某时段 t , 出租车 1 剩余电量为 20%, 则为了使出租车保持运营状态, 出租车 1 必须在 t 马上充电; 出租车 2 剩余电量为 30%, 则可运营时间为 $[t, t+1]$, 可充电时段为 t 和 $t+1$, 为保持运营状态, 必须至少从这 2 个时段中选择 1 个充电; 出租车 3 剩余电量为 40%, 则可运营时间为

$[t, t+2]$, 可充电时段为 $t, t+1, t+2$, 从这 3 个时段中至少选择 1 个充电可保证正常运营。

设出租车为恒功率充放电, 充电一个时段增加电量 E_h , 运营一个时段消耗电量 E_f , $E_h = \beta \times E_f$ ^[23], β 为比例系数。从中选择了一个时段充电以后, 出租车电池的剩余电量得到了更新, 下一个可运营区间也相应变化。

出租车每个时段的营业额 R_t 不同, 将 $R_t - R_{t'\min}$ ($t' \neq t, t' \in T$) 作为出租车在 t 时段不充电的经济激励 A_j , 其中 $R_{t'\min}$ 为除 t 时刻之外的其他时刻营业额的最小值。这里假设在相同收益下, 车主会放弃在当前时刻充电, 并假设车主会真实上报 A_j 。

聚合商将 n 个用户上报的单位电量激励值 A_m ($m=1, 2, \dots, n$) 从小到大排列, 计算出每个激励值下用户的充电量, 则可得到充电量—经济激励曲线, 其数学表达式为

$$x = \begin{cases} nP + x_{d0}, & A < A_{\min} \\ (n-k)P + x_d, & A_s \leq A < A_{s+1} \\ 0, & A \geq A_{\max} \end{cases} \quad (5)$$

$s = 1, 2, \dots, S$

式中: x 为充电负荷; A 为单位电量激励值; A_{\min} 、 A_{\max} 分别为经济激励的最小值和最大值; A_s 为第 s 个经济激励数据; n 为一开始准备充电的出租车数量; k 为放弃充电的出租车数量; S 为经济激励值的个数; P 为出租车的充电功率; x_{d0} 为响应激励之前的私家车负荷; x_d 为响应激励后的私家车负荷。

1.4 聚合商的最优充电调度模型

聚合商充电调度模型的决策变量为经济激励值和用户的充电量。由于实时电价由实时市场出清模型决定, 充电调度模型为一个二层模型: 上层以聚合商利润最大化为目标; 下层为以发电商成本最低为目标的市場出清模型, 该模型为

$$\max p x_t - \lambda_t x_t - k_t P A_t - (x_{d0} - x_{dt}) A_t \quad (6)$$

约束条件为

$$x_t = \begin{cases} n_t P + x_{d0} & A_t < A_{\min} \\ (n_t - k_t) P + x_{dt} & A_{ts} \leq A_t < A_{t(s+1)} \\ 0 & A_t \geq A_{\max} \end{cases} \quad (7)$$

$s = 1, 2, \dots, S$

$$k_t > 0 \tag{8}$$

式(6)中：第 1 项为聚合商的售电收入；第 2 项为购电成本；第 3 项为向响应激励的出租车用户所发放的激励成本；第 4 项为向响应激励的私家车用户发放的激励成本。

式(6)~(8)中： p 为零售电价； x_t 为 t 时刻总负荷； A_t 为 t 时刻的经济激励； A_s 为 t 时刻第 s 个经济激励数据； $A_{t(s+1)}$ 为 t 时刻第 $s+1$ 个经济激励数据； S 为经济激励值的个数； A_{\min} 、 A_{\max} 分别为 t 时刻经济激励的最小值和最大值； n_t 和 k_t 分别为 t 时刻原来准备充电的出租车数量和放弃充电的出租车数量； x_{d0} 为 t 时刻原计划要充电的私家车负荷； x_{dt} 为 t 时刻充电的私家车负荷； λ_t 由式(1)~(3)得到。

2 求解过程

实时市场出清模型的 KKT 条件为

$$c_{it} - \lambda_t - \omega_{it\min} + \omega_{it\max} = 0 \tag{9}$$

$$\sum_{i=1}^N q_{it} = x_t + D_t \tag{10}$$

$$0 \leq \omega_{it\max} \perp q_{it\max} - q_{it} \geq 0 \tag{11}$$

$$0 \leq \omega_{it\min} \perp q_{it} - q_{it\min} \geq 0 \tag{12}$$

上述(10)~(11)所示的 KKT 条件可通过引入二进制变量将其线性化为如下最优条件：

$$0 \leq \omega_{it\max} \leq M_{\omega\max} \theta_{\omega\max} \tag{13}$$

$$0 \leq q_{it\max} - q_{it} \leq M_{\omega\max} (1 - \theta_{\omega\max}) \tag{14}$$

$$0 \leq \omega_{it\min} \leq M_{\omega\min} \theta_{\omega\min} \tag{15}$$

$$0 \leq q_{it} - q_{it\min} \leq M_{\omega\min} (1 - \theta_{\omega\min}) \tag{16}$$

式中： $M_{\omega\max}$ 、 $M_{\omega\min}$ 为足够大的常数； $\theta_{\omega\max}$ 、 $\theta_{\omega\min}$ 为二进制变量。

模型目标函数中的 $\lambda_t x_t$ 为非线性项，可利用强对偶理论将其线性化。根据强对偶理论，原问题的目标函数等于对偶问题的目标函数，对于实时市场出清模型，即

$$\lambda_t (x_t + D_t) + \omega_{it\max} (-q_{it\max}) + \omega_{it\min} (q_{it\min}) = \sum_{i=1}^N (c_{it} q_{it}) \tag{17}$$

进一步可得

$$\lambda_t x_t = \sum_{i=1}^N (c_{it} q_{it}) - \omega_{it\max} (-q_{it\max}) - \omega_{it\min} (q_{it\min}) - \lambda_t D_t \tag{18}$$

式(18)所示等式右边的表达式为线性表达式。

x_t 为关于 A_t 的分段函数，为方便求解，将式

(7)变换为式(19)，其推导过程略。

$$k_t A_t = \sum_{u=2}^l y_{tu} (u-1) A_{t(u-1)} \tag{19}$$

式中： y_{tu} 为 0-1 变量， $y_{tu}=1$ 表示 A_t 在第 u 个区间， $y_{tu}=0$ 表示 A_t 不在第 u 个区间； l 为分段区间个数。由于 $u=1$ 时不进行激励，竞标模型是在需要激励时才进行计算，因此，式(19)中 u 从 2 开始。

至此，聚合商的竞标问题成为一个混合整数线性规划(MILP)问题。MILP 问题传统的求解方法是拉格朗日松弛法和次梯度法，缺点是计算量大且收敛慢。很多研究者提出分支切割法(branch and cut, BAC)，然而由于确定凸集的切割难以获得，复杂的问题仍需花费重大的计算代价。最近，Mikhail A. Bragin 等提出了拉格朗日松弛替代法^[24](surrogate lagrangian relaxation, SLR)，更新乘子时不需要得到所有子问题的最优解，收敛到最优解不需要知道最优对偶值，大大减少计算工作量。在求解过程中，拉格朗日乘子之间的距离在连续迭代中不断减少，最终收敛到唯一值。为了更加有效地利用分离性以及线性，Mikhail A. Bragin 等提出将 SLR 和 BAC 协同组合来求解 MILP 问题^[24]，其基本思想是利用 SLR 通过松弛耦合约束将问题分解成子问题，每个子问题的求解采用 BAC。求解过程中，子问题的相关约束局部地处理，不会影响整个问题，而且单个的子问题比原来的问题更容易获得有效的切割。

利用 SLR+BAC 方法求解本文提出的模型，其算法流程图如图 2 所示。

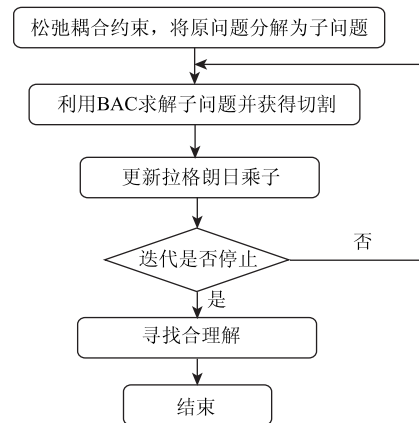


图 2 算法流程

Fig. 2 Flowchart of the algorithm

图2中,拉格朗日乘子的迭代公式略。

为求解该优化问题,将耦合约束条件(10)、(19)松弛化,引入拉格朗日乘子得到松弛化问题为

$$\begin{aligned} \max p x_t - \lambda_t x_t - \sum_{u=2}^l P y_{ut} (u-1) A_{t(u-1)} - \\ A_{t(u-1)} (x_{dt0} - x_{dt}) + \gamma_1 \left(\sum_{i=1}^N q_{it} - x_t - D_t \right) + \\ \gamma_2 \left(\sum_{u=2}^l y_{ut} - 1 \right) \end{aligned} \quad (20)$$

式中: γ_1 和 γ_2 为拉格朗日乘子,上述问题可分解成 $l-1$ 个子问题。

3 算例

设出租车电池容量为 60kWh, 剩余 SOC 均匀分布在(20%, 80%), 充电功率为 30kW, 耗电功率 10kWh, 营业额数据取自文献 [4], 设电池剩余 SOC 的下限值为 20%。假设实际接入的私家车比日前预测多了 250 辆, 其参数根据表 1 中的数据随机选取, 为简化分析, 设第 1 类用户占 20%, 第 2 类用户中 60% 的用户的期望电费支出减少率为 10%, 其余 40% 的用户期望电费支出减少率为 20%。计算时段为 1h。

表 1 电动私家汽车数据的概率分布

Table 1 Private electric vehicle parameters probability distribution

电动私家车参数	分布类型	均值	标准差	最小值	最大值
电池容量/kWh	均匀分布	18	6.93	6	30
初始 SOC/%	截尾正态分布	75	25	25	95
额定充电功率/kW	截尾正态分布	3.54	1.48	2	10

实时市场发电商的报价数据如表 2 所示, 发电商 4 为风力发电商, 其报价在一定范围内变化, 取风力发电商 4 种不同的报价参数代表 4 种不同的批发电价情形。实时市场的其他负荷数据取自文献 [14]。零售电价为 50USD/MWh。SLR 算法的迭代停止标准为对偶间隙大于 1%, BAC 算法的迭代停止标准为计算时间超过 10min, 算法利用 CLPEX 软件实现。

表 3 给出了批发电价为 50.57USD/MWh, 出租车数量为 160 辆时, 聚合商根据用户上报的激励值计算出的激励值为不同数值时对应的充电负荷, 表中给出的是部分数据。

表 2 发电商报价参数

Table 2 Parameters of generators

发电商	c/USD/MWh	最大值/MW
1	35	50
2	30	20
3	25	20
4	15~120	50

表 3 不同激励值时聚合商计算的充电负荷

Table 3 Charging loads calculated by aggregator with different incentive values

激励 USD/MWh	充电负荷/kW	激励 USD/MWh	充电负荷/kW
0	5 548.2	7.78	4 273.5
2.23	5 200.3	9.29	3 733.9
4.15	5 099.1	11.11	3 564.1
6.06	4 862.3	13.59	3 200.5

表 4 给出了批发电价和出租车数量不同的情形下, 不实施需求响应项目和实施经济激励的需求响应项目时的实时电价、经济激励总额、出租车和私家车充电负荷以及聚合商收益的计算结果, 收益指收入减去成本。共分析了 4 种情形: 情形 1 为实时批发电价较低的情形; 情形 2 为批发电价稍高的情形; 情形 3 为批发电价较高的情形; 情形 4 为批发电价很高且出租车数量较大时的情形。

表 4 计算结果

Table 4 Computational results of the model

情形	电价 USD/MWh	激励 USD/MWh	出租车负荷/kW	私家车负荷/kW	聚合商收益/USD
1	30/30	0	3 840/3 840	748.2/748.2	91.8/91.8
2	35.14/31.75	5.81	4 800/4 200	748.2/748.2	82.5/87.1
3	50.57/42.63	9.25	4 800/3 120	748.2/621.4	-3.2/10.9
4	64.79/54.52	11.40	5 760/3 840	748.2/518.9	-85.2/-43.7

表 4 中, “无” 表示没有基于激励的需求响应项目, “有” 表示会在需要时进行激励。

结果表明, 当实时批发电价较低(情形 1)时, 聚合商没有动力进行激励; 当实时批发电价较高(情形 2 至情形 4)时, 聚合商会进行激励。进行经济激励后, 负荷减少, 批发电价降低, 聚合商的收益提高。

为了分析采用本文方法后, 整个调度周期(1

天内聚合商的收益,表5给出了采用基于经济激励的需求响应后,1天内聚合商收益并与无需求响应的情况进行比较。为简化分析,设计算的起始时刻有160辆出租车接入,其他时刻均未有新的出租车接入。

表5 整个调度周期内聚合商收益比较

Table 5 Aggregator revenue comparison in the whole scheduling cycle

	无需求响应	激励型需求响应
聚合商收益/USD	351.5	426.8

从表5可以看出,基于激励的需求响应方法使整个调度周期内聚合商的收益大于无需求响应的情况。

4 结 论

研究了电动汽车聚合商如何决策最优的经济激励和充电量以获得收益最大化。利用算例对所提模型的有效性和正确性进行了验证和分析,并与不实施需求响应的情形做了对比,结果表明基于经济激励的需求响应可以提高聚合商收益。

研究的前提是假设电动汽车放电模型为线性放电模型,实际中电动汽车耗电量受车况和路况等多种因素的影响,是时变的,因此本文下一步的研究工作为建立更接近实际情况的电动汽车放电模型,并在该模型的基础上研究聚合商的最优充电调度。

参 考 文 献

- [1] 徐智威,胡泽春,宋永华,等. 基于动态分时电价的电动汽车充电站有序充电策略[J]. 中国电机工程学报,2014,34(22):3638-3646.
XU Zhiwei, HU Zechun, SONG Yonghua, et al. Coordinated charging strategy for PEV charging stations based on dynamic time-of-use tariffs [J]. Proceedings of the Csee, 2014, 34(22): 3638-3646.
- [2] 张晓萱,薛松,杨素,等. 售电侧市场放开国际经验及其启示[J]. 电力系统自动化,2016,40(9):1-8.
ZHANG Xiaoxuan, XUE Song, YANG Su, et al. International experience and lessons in power sales side market liberalization [J]. Automation of Electric Power Systems, 2016, 40(9): 1-8.
- [3] 陈启鑫,刘敦楠,林今,等. 能源互联网的商业模
- 式与市场机制(一)[J]. 电网技术,2015,39(11):3050-3056.
CHEN Qixin, LIU Dunnan, LIN Jin, et al. Business models and market mechanisms of energy internet(1) [J]. Power System Technology, 2015, 39(11): 3050-3056.
- [4] YANG Z, SUN L, KE M, et al. Optimal charging strategy for plug-In electric taxi with time-varying profits [J]. IEEE Transactions on Smart Grid, 2014, 5(6): 2787-2797.
- [5] 张维戈,陈连福,黄彧,等. M/G/k 排队模型在电动出租车充电站排队系统中的应用[J]. 电网技术,2015,39(3):724-729.
ZHANG Weige, CHEN Lianfu, HUANG Yu, et al. Application of M/G/k queuing model in queuing system of electric taxi charging station [J]. Power System Technology, 2015, 39(3): 724-729.
- [6] 李亚芬,黄梅,张维戈. 电动出租车日充电负荷估算方法[J]. 电力系统自动化,2014,38(10):55-60.
LI Yafen, HUANG Mei, ZHANG Weige. An estimation method for daily charging load of electric taxis [J]. Automation of Electric Power Systems, 2014, 38(10): 55-60.
- [7] 刘洪,李荣,葛少云,等. 考虑出租车随机行为特性及路网行程时间可靠性的充电站多目标规划[J]. 电网技术,2016,40(2):433-441.
LIU Hong, LI Rong, GE Shaoyun, et al. Multiple objective planning for electric taxi charging station considering random-probability behavioral trait of taxi and travel time reliability [J]. Power System Technology, 2016, 40(2): 433-441.
- [8] 葛少云,李荣,韩俊,等. 考虑电动出租车随机概率行为特性的充电站规划[J]. 电力系统自动化,2016,40(4):50-58.
GE Shaoyun, LI Rong, HAN Jun, et al. Charging station planning considering probability behavior characteristic of electric taxi [J]. Automation of Electric Power Systems, 2016, 40(4): 50-58.
- [9] 杨亚雄,杨洪明,张俊. 电动汽车聚合商商电力市场竞争策略研究[J]. 电力科学与技术学报,2015,30(2):104-110.
YANG Yaxiong, YANG Hongming, ZHANG Jun. Research on bidding strategy of electricity market for electric vehicle aggregators [J]. Journal of Electric Power Science and Technology, 2015, 30(2): 104-110.

- [10] SUNDSTROM O, BINDING C. Flexible charging optimization for electric vehicles considering distribution grid constraints [J]. IEEE Transactions on Smart Grid, 2012, 3(1): 26 - 37.
- [11] PANTOS M. Exploitation of electric-drive vehicles in electricity markets [J]. IEEE Transactions Power System, 2012, 27(2): 682 - 694.
- [12] BESSA R J M, MATOS A, SOARES F J, et al. Optimized bidding of a EV aggregation agent in the electricity market [J]. IEEE Transactions on Smart Grid, 2012, 3(1): 443 - 452.
- [13] BESSA R J, MATOS M A. Global against divided optimization for the participation of an EV aggregator in the day-ahead electricity Marke Part I: theory [J]. Electric Power System Research, 2013(95): 309 - 318.
- [14] BESSA R J, MATOS M A. Optimization models for EV aggregator participation in a manual reserve market [J]. IEEE Transactions on Power Systems, 2013, 28(4): 4031 - 4041.
- [15] CARAMANIS M C, FOSTER J M. Optimal power market participation of plug-in electric vehicles pooled by distribution feeder [J]. IEEE Transactions on Power Systems, 2013, 28(3): 3085 - 3095.
- [16] MADSEN P H. Pool strategy of a price-maker wind power producer [J]. IEEE Transactions on Power Systems, 2013, 28(3): 3440 - 3450.
- [17] KRISTOFFERSEN T K, Capion K, Meibom P. Optimal charging of electric drive vehicles in a market environment [J]. Applied Energy, 2011, 88(5): 1940 - 1948.
- [18] VAGROPOULOS S I, BAKIRTZIS A G. Optimal bidding strategy for electric vehicle aggregators in electricity markets [J]. IEEE Transactions on Power System, 2013, 28(4): 4031 - 4041.
- [19] MARINA G V, ERSSON G. Optimal bidding strategy of a plug-in electric vehicle aggregator in day-ahead electricity markets under uncertainty [J]. IEEE Transactions on Power Systems, 2015, 30(5): 2375 - 2386.
- [20] 宫鑫, 林涛, 苏秉华. 电动汽车代理在电力市场的最优竞标策略 [J]. 电网技术, 2016, 40(9): 2596 - 2602.
- GONG Xin, LIN Tao, SU Binghua. Optimal bidding strategy of a electric vehicle aggregator in electricity market [J]. Power System Technology, 2016, 40(9): 2596 - 2602.
- [21] FANG X, HU Q, LI F, et al. Coupon-based demand response considering wind power uncertainty: a strategic bidding model for load serving entities [J]. IEEE Transactions on Power Systems, 2016, 31(2): 1025 - 1037.
- [22] ZHONG H, XIE L, XIA Q. Coupon incentive-based demand response (CIDR) in smart grid [C] // IEEE Power & Energy Society General Meeting, San diego, IEEE, 2012: 1 - 6.
- [23] YANG Z Y, SUN L H, CHEN J M, et al. Profit maximization for plug-in electric taxi with uncertain future electricity prices [J]. IEEE Transactions on Power Systems, 2014, 29(6): 3058 - 3068.
- [24] BRAGIN M A, LUH P B, YAN J H. Novel exploitation of convex hull invariance for solving unit commitment by using surrogate lagrangian relaxation and branch-and-cut [C] // Power & Energy Society General Meeting, Denver, IEEE, 2015: 1 - 5.

收稿日期: 2018-09-12

作者简介:

宫鑫(1980—), 女, 硕士, 讲师, 研究方向为电动汽车与电网互动、电力市场等, E-mail: 26551848@qq.com;

苏禹(1979—), 男, 博士, 副教授, 研究方向为电力系统自动化等, E-mail: 987654@qq.com;

张小凤(1982—), 女, 博士, 讲师, 研究方向为电力系统自动化等, E-mail: 496537140@qq.com;

黄相杰(1986—), 男, 硕士, 讲师, 研究方向为人工智能等, E-mail: 67019902@qq.com.

(责任编辑: 宋书芳)

基于单片机的激光二极管温度控制研究

喻武龙¹

(北京理工大学珠海学院, 广东, 珠海, 519085)

摘要: 激光二极管对温度具有高精度、超调量小等特点, 被广泛应用于各领域中, 其性能受运行温度影响较为严重, 需要保证其工作温度的恒定。因此深入研究基于单片机的激光二极管温度控制方法, 以 MSP430F449 单片机和半导体制冷片作为主控制器和制冷器, 通过温度采集电路采集激光二极管当前温度, 用阻值表示, 仪表放大器将阻值转化为电压值, 同单片机控制器设定的电压值对比, 获取温度差值信号; 单片机控制器采用 PID 控制算法处理温度差值信号后, 利用定时器生成脉冲宽度调制模式输出电压, 电压由驱动电路进入制冷器内产生电流, 制冷器按照电流通方向, 对激光二极管进行制冷或加热, 完成激光二极管温度控制。实验结果表明, 此方法温度控制误差低于 0.03°C, 且温度控制响应时间为 30s, 优于对比方法。

关键词: 单片机; 激光二极管; 温度控制; 温度采集; 半导体制冷片; PID 算法

中图分类号: TP273

文献标识码: A

Research on Laser Diode Temperature Control Based on Single Chip Microcomputer

Yu-Wulong¹

(1. Beijing Institute of Technology, Zhuhai, Guangdong Zhuhai 519085, China)

Abstract: Laser diode is widely used in various fields because of its high accuracy and small overshoot. Its performance is seriously affected by the operating temperature. It is necessary to ensure the constant working temperature. Therefore, the temperature control method of laser diode based on MCU is deeply studied. MSP430F449 MCU and semiconductor chiller are used as main controller and cooler. The current temperature of laser diode is collected by temperature acquisition circuit. The resistance value is expressed by resistance value. The instrument amplifier converts resistance value into voltage value, and compares it with the voltage value set by MCU controller to obtain temperature difference signal. After processing the temperature difference signal with PID control algorithm, the output voltage of pulse width modulation mode is generated by timer. The voltage is generated by driving circuit into the cooler, and the cooler refrigerates or heats the laser diode according to the direction of current flow to complete the temperature control of the laser diode. The experimental results show that the temperature control error of this method is less than 0.03 C, and the response time of temperature control is 30 s, which is better than the contrast method.

Key words: MCU; Laser Diode; Temperature Control; Temperature Collection; Semiconductor Refrigerator; PID Algorithms

1 引言

作为光纤通信系统内主要的光源, 激光二极管不仅具有效率高、易于调制的优势, 同时还具有体积小、结构简单、成本低等特点^[1], 因此被广泛应用于激光测距、光信息处理和激光引信等领域中。激光二极管的工作过程中, 会将少量电能转变为热能, 造成激光二极管的温度上升与波动, 导致其出光性能受到较大影响^[2]。根据以往的相关研究可知, 当激光二极管温度上升时, 其阈值电流也随之上升, 其出光功率在驱动电源恒定的状态下也随之上升; 激光二极管温度上升时, 其出射光波有较高概率出现约 0.9nm/°C 的红移现象^[3], 导致固定条件下波长无法达到所设标准。同时激光二极管的工作寿命及输出功率均与其温度的波动存在直接关系^[4]。为了提升激光二极管的输出精度与稳定性, 同时延长其工作寿命, 需要精确控制激光二极管的运行温度。

由控制器、运算器以及存储器等组成的单片机在功能上与计算机相似, 具有体积小, 成本低、可置于机器内部等优势, 是具有代表性的微控制器^[5,6]。因此, 提出基于单片机的激光二极管温度控制方法, 以单片机和半导体制冷片分别作为主控制器和制冷器, 通过 PID 控制算法控制电压输出, 利用制冷器快速精准的控制激光二极管温度。

2 基于单片机的激光二极管温度控制

基于单片机的激光二极管温度控制过程主要分为温度采样和单片机控制两部分^[7], 通过温度采集电路采集激光二极管当前温度, 以电阻值表示, 利用桥式电路与仪表放大器将电阻值转变成电压值, 此电压值与主控制器给定的控制电压值相比较, 获取温度差值信号; 以 MSP430F449 单片机作为主控制器, 采用 PID 控制算法处理温度差值信号后, 利用定时器生成脉冲宽度调制模

式输出电压，电压由驱动电路进入半导体制冷片内产生电流，半导体制冷片按照电流流通方向，对激光二极管进行制冷或加热，完成激光二极管温度控制。图 1 为激光二极管温度控制过程。

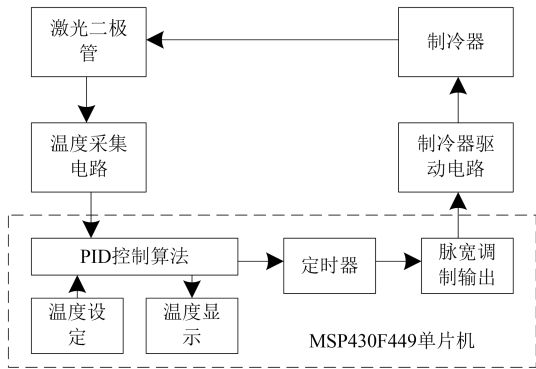


图 1 激光二极管温度控制过程

2.1 温度采样

基于单片机控制激光二极管温度时，需要先通过温度采集电路采集激光二极管当前的温度，根据采集的温度结果进行温度控制，温度采集电路如图 2 所示。温度采集电路由热敏电阻器、专用仪表放大器、数模转换器、减法器构成^[8]。通过具有负温度系数的热敏电阻采集激光二极管当前温度，当激光二极管温度上升时，热敏电阻的阻值下降^[9]；利用桥式电路与仪表放大器 AD620 可将负温度系数热敏电阻的阻值转变成电压值，传输至主控制器内。对比此电压值与主控制器给定的控制电压值，获取温度差值信号，根据温度差值信号得到温度误差。

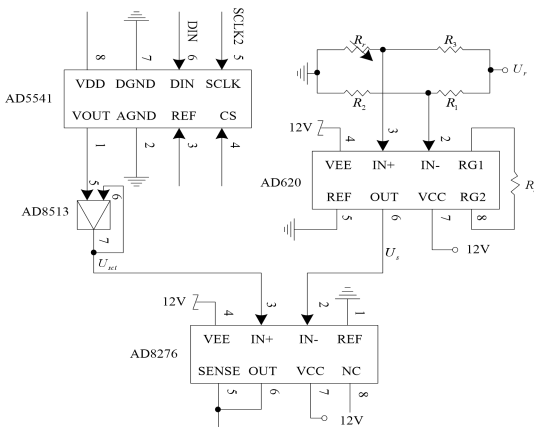


图 2 温度采集电路

数模转换器在温度采集过程中的主要作用是通过连接模拟控制电路和数字控制电路，实现数字电压与模拟电压的转换^[10]。数模转换器选择 16 位低功耗 DAC 转换芯片 AD5541 与 DSP 芯片，DAC 转换芯片采用三线串行控制方式，DSP 芯片的 SPI 结构作为连接中心连接 DAC 转换芯片和单片机控制器。通过电阻同具有负温度系数的热敏电阻组成的桥式结构同专用仪表放大器 AD620 相连。减法器采用 AD8276 芯片，其内部具有 4 个激光刻蚀技术集成的温度特性匹配电阻，在无外围电路条件下完成电阻计算。

桥式电路内的除热敏电阻外的其他电阻均采用温

度漂移系数一致的精密电阻，以降低模拟电路控制精度受外部温度变化的影响，提升激光二极管温度采集的精度。热敏电阻同仪表放大器 AD620 间的关系通过式 (1) 描述：

$$U_s = \left(1 + \frac{49.4}{R_h}\right) \left(\frac{R_r U_r}{R_r + R_3} - \frac{R_2 U_r}{R_1 + R_2}\right) \quad (1)$$

式 (1) 内， U_s 为温度输出电压； R_r 和 R_1 、 R_2 、

R_3 分别为桥式电路内的热敏电阻和其他电阻的阻值；

U_r 为阻值转变的电压值； R_h 为 R_1 、 R_2 、 R_3 阻值的和。

当 $R_1 = R_2 = 10\text{k}\Omega$ ， $R_3 = 4.9\text{ k}\Omega$ 时， R_h 值为 $25\text{k}\Omega$ ， U_r 为

5V，此时 U_s 值如下：

$$U_s \approx 3 \left(\frac{R_r}{R_r + 5.1} - 0.5\right) U_r \quad (2)$$

仪表放大器中共包含三个运算放大器，桥式电路各路输出均传输至运算放大器的正输入端^[11]。由于运算放大器正输入端的输入阻抗约为无穷大，因此热敏电阻变化受后端电路影响程度可降至最低。同时 AD620 的电压噪声密度和温漂系数均低于同类型机器的平均水平，且具有简易的外围电路，通过一个外接电阻即可调整电路放大倍数、抑制极高共模电压。

2.2 制冷器控制与驱动

以 MSP430F449 单片机作为激光二极管温度控制的主控制器，以半导体制冷片作为制冷器^[12,13]，主控制器的功能为采用 PID 控制算法处理温度差值信号，并利用不同占空比的电压控制驱动电路。

制冷器的驱动模式分别两种，分别是以波纹小为优势的线性模式和以低功耗、低散热、高电源效率为优势的脉冲宽度调制模式^[14]。制冷器采用线性模式驱动过程中，功率三极管于线性区运行，输入电压控制输出电流，此驱动模式下制冷器的效率较低，散热量较大。制冷器采用脉冲宽度调制模式驱动过程中，场效应管运行在开关状态，脉冲信号的占空比控制输出电流的方向和大小，此驱动模式下制冷器中含有噪声，需进行滤波以降低波纹电压。基于上述分析，在控制激光二极管温度时，制冷器选取脉冲宽度调制模式驱动。MSP430F449 单片机的定时器生成制冷器驱动的脉冲宽度调制模式，以修正定时寄存器的值实现脉冲宽度调制模式占空比的变化^[15]，选取连续增计数模式作为计数方式。驱动器电路图如图 3 所示

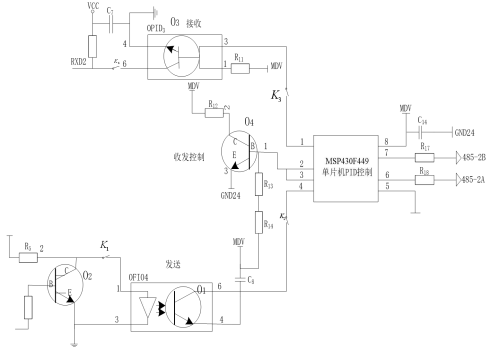


图3 驱动器电路图

制冷器通过 H 桥式驱动电路获取双向、大小精密可调的驱动电流^[16]。用 O 和 K 分别表示驱动电路中的电平和开关，若 O_1 与 O_2 为高电平， O_3 与 O_4 为低电平，那么 K_1 与 K_2 开启， K_3 与 K_4 断开，电流在制冷器中由左至右流通；若 O_1 与 O_2 低电平， O_3 与 O_4 为高电平，那么 K_1 与 K_2 断开， K_3 与 K_4 开启，电流在制冷器中由右至左流通。利用 MSP430F449 单片机 PID 控制 O_1 或 O_4 的脉冲宽度调制模式占空比，基于 K_1 或 K_4 开启时间的控制实现制冷器运行时间的控制，最终实现激光二极管温度控制的目的。

2.3 单片机的控制原理与特点

比例、积分、微分控制简称 PID 控制，其具有控制精度高、稳定性好、结构简单、可调节等优势^[17]。在缺乏精确的数学模型，控制器的结构与参数需根据经验及现场调试获取时，PID 控制算法最为适用，因此在以单片机作为控制器控制激光二极管温度时，单片机采用 PID 控制算法进行控制。

激光二极管温度控制的核心是单片机 PID 控制算法的参数整定，判断 PID 控制算法比例系数、积分时间与微分时间大小的依据是激光二极管温度控制过程的特性。单片机 PID 控制算法的参数整定方法分为理论计算整定和工程整定两种^[18]，其中理论计算整定是按照给定的数学模型，通过理论计算获取控制参数；工程整定是按照以往的工程经验，直接进行控制实验。理论计算整定获取的参数与工程实际情况具有一定差距，需进行修正后才可使用，而工程整定法过程简单，易掌握，是实际控制应用中使用较广泛的方法。

在基于单片机的激光二极管温度控制过程中，单片机 PID 控制算法的一般算式为：

$$u(y) = L_c \left[e(y) + \frac{1}{Y_I} \int_0^y e(y) dy + Y_D \frac{de(y)}{dy} \right] \quad (3)$$

式 (3) 内， $u(y)$ 和 $e(y)$ 分别表示第 y 次控制时

单片机输出和温度误差； L_c 、 Y_I 和 Y_D 分别为单片机的放大系数（比例增益）、积分常数和微分时间常数。单片机 PID 控制算法的原理就是通过修正 L_c 、 Y_I 和 Y_D 三个参数，提升激光二极管温度控制性能。

因为采用单片机作为控制器控制激光二极管温度的过程，实质上是一种采样控制过程^[19]，是依照温度采集时刻的温度误差确定控制量。所以在单片机通过 PID 控制算法控制激光二极管温度时，需离散化处理式 (3)，将微分方程转化为数字形式的差分方程，这个过程中可通过求和与增量式描述积分项与微分项：

$$\frac{de(y)}{dy} \triangleq \frac{E(L) - E(L-1)}{\Delta y} = \frac{E(L) - E(L-1)}{Y} \quad (4)$$

$$\int_0^y e(y) dy = \sum_{j=0}^n E(j) \Delta y = Y \sum_{j=0}^n E(j) \quad (5)$$

上述公式内， $\Delta y = Y$ ，表示温度采样周期； $E(L)$

和 $E(L-1)$ 分别表示第 L 次和 $L-1$ 次温度采样过程中的偏差值

在式 (3) 内，融入式 (4) 和式 (5)，获取离散的 PID 算法表达式：

$$P(L) = L_p \left\{ E(L) + \frac{Y}{Y_I} \sum_{j=0}^n E(j) + \frac{Y_D}{Y} [E(L) - E(L-1)] \right\} \quad (6)$$

式 (6) 内 $P(L)$ 表示第 L 次温度采样时单片机的

输出，为保证 $P(L)$ 的精度，需使 Y 足够小。

3 实验分析

3.1 性能测试实验

实验以某型号激光二极管作为实验对象，从电路角度和激光二极管输出光谱两方面进行实验，以验证本文方法的有效性，结果如下。

3.1.1 电路测试实验

实验开始前，采用 MSP430F449 单片机控制器将实验对象的运行温度设置为 22°C ，环境温度高于实验对象运行温度 5°C 左右。记录采用本文方法后，实验对象运行温度随时间变化的曲线，结果如图 4 所示。

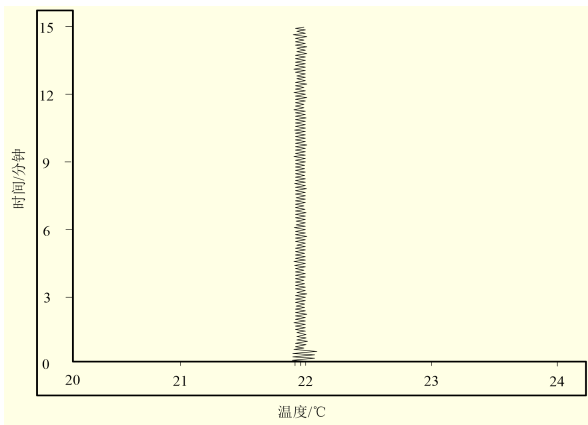
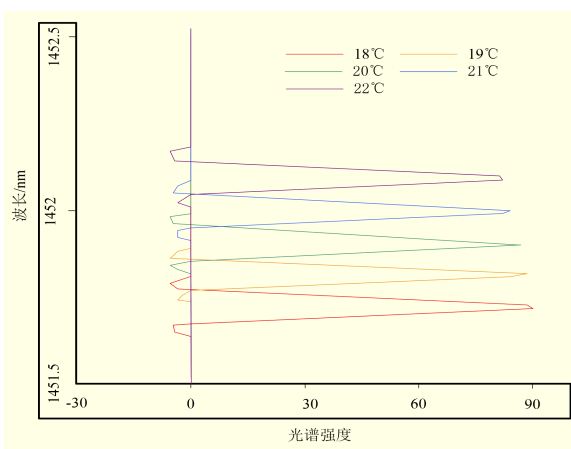


图4 电路测试结果

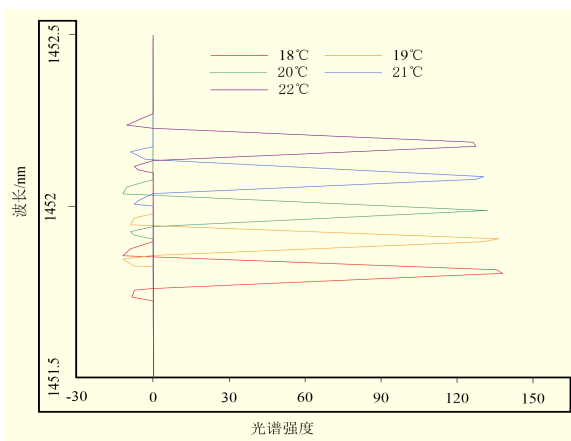
分析图4中的实验数据得到,采用本文方法后,实验对象的运行温度在0.5分钟后达到单片机控制器设置的温度值。15分钟的持续观察可知,实验对象的运行温度在达到设置温度后,运行温度的变化范围控制在 -0.03°C — 0.03°C 内,未产生明显的跳变现象。实验结果表明本文方法能够稳定控制激光二极管的温度。

3.1.2 激光二极管输出光谱测试

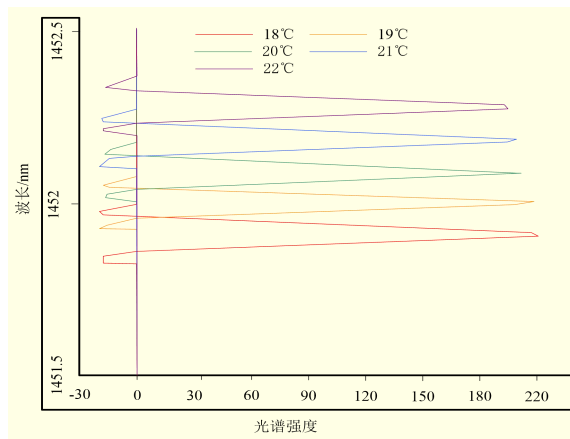
采用本文方法控制实验对象运行温度时,通过傅里叶红外光谱仪测量实验对象的输出光谱。将实验对象的注入电流分别设定为30mA、50mA和70mA,采用本文方法将实验对象的运行温度控制在 18°C — 22°C 下,分别测量实验对象的输出光谱,结果如图5所示。



(a) 电流为30mA时实验对象的输出光谱



(b) 电流为50mA时实验对象的输出光谱



(c) 电流为70mA时实验对象的输出光谱

图5 实验对象的输出光谱图

分析图5的实验结果得到,随着实验对象运行温度的逐渐提升,其输出光谱的峰值波长也逐渐上升。在电流为30mA条件下,随着实验对象运行温度由 18°C 上升至 22°C 时,波长峰值由1451.60nm上升至1451.98nm;在电流为50mA条件下,随着实验对象运行温度由 18°C 上升至 22°C 时,波长峰值由1451.64nm上升至1452.04nm;在电流为70mA条件下,随着实验对象运行温度由 18°C 上升至 22°C 时,波长峰值由1451.77nm上升至1452.15nm。将不同电流值条件下,随着实验对象运行温度提升,其输出波长的变化情况用图6描述。

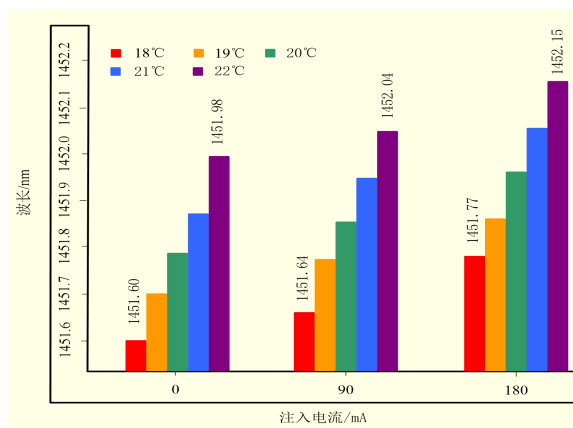


图6 输出波长同运行温度和注入电流的关系

分析图6得到,采用本文方法后,随着注入电流的提升,实验对象不同运行温度的输出波长也逐渐提升,实验对象温度调谐系数的波动范围控制在 $0.09\text{nm}/^{\circ}\text{C}$ 左右。

3.2 性能对比实验

分别采用本文方法,基于温漂补偿的激光二极管温度控制方法和基于水冷散热的激光二极管温度控制方法控制实验对象温度,分别从控制精度与响应时间两方面对比不同方法,结果如下所示。

3.2.1 控制精度对比

将实验对象的运行温度分别设置为 22°C 、 25°C 、 28°C 、 30.3°C 、 33.7°C 、 38.5°C ,采用不同控制方法控制实验对象的温度,5分钟后测量不同方法控制下实验对象的运行温度,对比不同控制方法的绝对误差,验证本

文方法的控制精度，结果如表 1 所示。

表 1 不同方法的控制精度对比结果

本文方法			
序号	设定温度/°C	实测温度/°C	绝对误差/°C
1	22	21.99	0.01
2	25	25	0
3	28	28.02	-0.02
4	30.3	30.27	0.03
5	33.7	33.7	0
6	38.5	38.51	-0.01

基于温漂补偿的控制方法			
序号	设定温度/°C	实测温度/°C	绝对误差/°C
1	22	21.76	0.24
2	25	25.33	-0.33
3	28	28.19	-0.19
4	30.3	30.06	0.24
5	33.7	33.95	-0.25
6	38.5	38.23	0.27

基于水冷散热的控制方法			
序号	设定温度/°C	实测温度/°C	绝对误差/°C
1	22	22.02	-0.02
2	25	25.07	-0.07
3	28	27.88	0.12
4	30.3	30.51	-0.21
5	33.7	33.34	0.36
6	38.5	39.02	0.52

分析表 1 得到，采用本文方法控制实验对象运行温度时，温度控制的绝对误差在 0°C—0.03°C 之间；采用基于温漂补偿的控制方法控制实验对象运行温度时，温度控制的绝对误差在 0.19°C—0.33°C 之间；采用基于水冷散热的控制方法控制实验对象运行温度时，初始阶段的绝对误差较低，仅为 0.02°C，而随着温度的提升，温度控制的绝对误差达到 0.52°C。实验结果表明，本文方法温度控制的精度更高。

3.2.2 控制响应时间对比

将实验对象的运行温度设置为 20°C，采用不同控制方法控制实验对象的运行温度，每 10s 进行一次测量，对比不同控制方法达到控制器设定温度的响应时间，结果如表 2 所示。

表 2 不同方法的控制响应时间对比

本文方法	基于温漂补偿的控制方法		基于水冷散热的控制方法	
	测量时间/s	实测温度/°C	测量时间/s	实测温度/°C
10	24.45	25.33	10	24.96
20	22.93	23.60	20	24.50

30	20.03	30	22.06	30	23.92
40	20.02	40	20.75	40	22.34
50	19.97	50	20.16	50	21.55
60	19.99	60	20.02	60	20.43
70	20.01	70	19.97	70	20.04
80	20.00	80	19.93	80	20.02
90	20.02	90	19.99	90	19.95
100	20.01	100	20.05	100	19.82
110	20.02	110	20.03	110	20.09
120	20.00	120	20.06	120	20.16
130	19.98	130	20.07	130	20.21
140	19.98	140	20.12	140	20.04
150	20.00	150	19.78	150	20.07
160	20.03	160	19.85	160	19.76
170	20.01	170	20.12	170	19.89
180	20.02	180	20.08	180	20.11

分析表 2 得到，本文方法控制实验对象运行温度 30s 后，实验对象的温度达到控制器设定温度，且在其后的 150s 观测时间内，温差波动较小；而其他两种控制方法分别在 60s 和 70s 后才达到控制器设定温度，且在其后的观测时间内，温差波动较大。实验结果说明本文方法控制响应时间较快。

4 结论

本文以 MSP430F449 单片机作为激光二极管温度控制的主控制器，通过温度采集电路采集激光二极管当前温度，获取温度误差；单片机控制器采用 PID 控制算法处理温度采集电路获取的温度差值信号后，利用制冷器对激光二极管进行制冷或加热，完成激光二极管温度控制。本文方法温度控制的绝对误差在 0°C—0.03°C 之间，明显低于传统方法；本文方法控制实验对象运行温度 30s 后，实验对象的温度达到控制器设定温度。实验验证本文方法具有较高的温度控制精度和稳定性，且控制响应时间较快，满足激光二极管温度控制要求。

参考文献

- [1] 高恒, 贾凯, 杨闯, 等. 激光二极管侧面抽运免温控激光器的研究[J]. 激光技术, 2019, 43(1):1-1.
- [2] 廖柯, 刘刚明, 周勇, 等. 基于内置光栅的大功率激光二极管[J]. 半导体光电, 2015, 36(6):869-874.
- [3] 田海军, 杨婷, 赵杨辉. 高精度脉冲式激光测距系统的设计[J]. 机床与液压, 2017, 45(3):118-122.
- [4] 薛竣文, 方宇杰, 谢海军, 等. 基于 PA92 的 F—P 扫描干涉仪设计[J]. 光学技术, 2016, 42(3):278-280.
- [5] 黄文发, 李学春, 王江峰, 等. 激光二极管抽运氦气冷却铍玻璃叠片激光放大器热致波前畸变和应力双折射的数值模拟和实验研究[J]. 物理学报, 2015, 64(8):318-326.
- [6] 陈晓, 贾华宇, 郭燕. 基于单片机的激光发生器的驱动电路设计[J]. 应用光学, 2015, V36(1):134-139.
- [7] 江金光, 唐亚男, 李姗姗. 基于单片机的晶振温度补偿

系统设计[J]. 压电与声光, 2016, 38(3):492-496.

[8] 井红旗, 仲莉, 倪羽茜,等. 高功率密度激光二极管叠层散热结构的热分析[J]. 发光学报, 2016, 37(1):81-87.

[9] XU JJ, CHEN C, YANG HJ, et al. Temperature control system for diode laser based on PID control and genetic-algorithm[J]. Journal of Shenyang University of Technology, 2017, 39(4):449-453.

[10] 郭丽萍, 张艳荣, 林思苗. 基于 AVR 单片机的激光电源闭环控制系统设计[J]. 中国测试, 2017, 43(3):78-82.

[11] 杜雪原, 粟荣涛, 王小林,等. 工作温度对光纤激光器输出特性的影响研究[J]. 中国激光, 2015, 42(b09):20-26.

[12] 周旭阳, 王劲松, 梁旭,等. 基于 LiB3O5 晶体腔内倍频的 126 W 高稳定性 532 nm 声光调 Q 激光器[J]. 激光与光电子学进展, 2018, 55(5):247-253.

[13] WANG Y. Chip-Level Packaging of Edge-Emitting Laser Diodes Onto Low-Cost Transparent Polymer Substrates Using Optodic Bonding[J]. IEEE Transactions on Components Packaging & Manufacturing Technology, 2016, 6(5):667-674.

[14] 颜佩琴, 孟文东, 王煜蓉,等. 基于温漂自动补偿的高稳定性 Si-APD 单光子探测器[J]. 激光与光电子学进展, 2017, 54(8):82-88.

[15] 李锐君, 李刚. 机械常减压机组温度优化控制研究[J]. 计算机仿真, 2016, 33(6):335-339.

[16] 金佳, 李佛生, 马宁生,等. 激光二极管的阈值电流与光谱特性研究[J]. 物理与工程, 2017, 27(5):110-113.

[17] 杨红伟, 彭海涛. 808nm 大功率激光二极管随机失效分析[J]. 微纳电子技术, 2015, 52(5):273-277.

[18] 赵萌, 李隆, 潘晓瑞,等. LD 双端泵浦 Nd : YAG 方形晶体热容激光器温度场 [J]. 激光与红外, 2018, v.48 : No.477(6):45-51.

[19] GUO YL, HUANG X, HONG Y, et al. Carbon Monoxide Measurement at Elevated Temperature Based on Tunable Diode Laser Absorption Spectroscopy[J]. Chinese Journal of Analytical Chemistry, 2015, 43(8):1247-1254.

基金项目:

广东省青年创新人才项目(2016KQNCX204)资助

作者简介: 喻武龙 (1979—), 男 (汉族), 江西抚州人, 硕士, 副教授, 主要研究方向: 单片机控制、网络通信。

联系方式: 广东省珠海市唐家湾金凤路 6 号北京理工大学珠海学院, 邮编: 519085, 邮箱: drags@163.com, 手机: 18575612161.